SEPARATRIX MAP ANALYSIS FOR FRACTAL SCATTERINGS IN WEAK INTERACTIONS OF SOLITARY WAVES

YI ZHU[*], RICHARD HABERMAN [†], AND JIANKE YANG [‡]

Abstract. Previous studies have shown that fractal scatterings in weak interactions of solitary waves in the generalized nonlinear Schrödinger equations are described by a universal second-order separatrix map. In this paper, this separatrix map is analyzed in detail, and hence a complete characterization of fractal scatterings in these weak interactions is obtained. In particular, scaling laws of these fractals are derived analytically for different initial conditions, and these laws are confirmed by direct numerical simulations. In addition, an analytical criterion for the occurrence of fractal scatterings is given explicitly.

Key words. weak interactions, solitary waves, fractal scattering, separatrix map.

1. Introduction. Solitary wave interactions are important phenomena in science and engineering [1, 2]. These interactions can be divided roughly into two types depending on the strength of the interactions. Strong interactions, often called collisions, are the interactions of solitary waves at close distance. They would occur when two solitary waves are initially far apart but move toward each other at moderate or large speeds. Weak interactions are the interactions of solitary waves at far distance through weak tail overlap. These interactions would occur if the two waves are initially well separated, and their relative velocities are small or zero. In integrable systems, collisions of solitary waves are elastic [1], and their weak interactions exhibit interesting but still simple behaviors [2, 3, 4, 5, 6]. For certain integrable systems perturbed by higher-order corrections, if they can be asymptotically transformed to integrable equations, then their solitary wave interactions would closely resemble those in integrable systems [7, 8, 9]. If the systems are non-integrable, however, solitary wave interactions can be extremely complicated, and they can depend on initial conditions in a sensitive, fractal manner. This fractal-scattering phenomenon was first discovered for kink and antikink collisions in the ϕ^4 model [10, 11, 12], later in several other physical systems as well [13, 14]. For these strong interactions, a resonant energy exchange mechanism between the collision and internal/radiation modes was found responsible for this fractal scattering. To analyze these fractal scatterings, approximate collective-coordinate ODE models based on variational methods [15] have been derived, and these ODEs are found to exhibit qualitatively similar fractal scatterings as in the PDEs [12, 16, 17, 18]. Goodman and Haberman further studied these collective-coordinate ODE models using dynamical systems methods [19, 20, 21, 22, 28]. Performing asymptotic analysis along separatrix (homoclinic) orbits, they derived separatrix maps which led to the prediction of n-bounce resonance windows. It is noted that the separatrix maps derived in [19, 20, 21, 22, 28] contain parameters which depend on initial conditions. In addition, these maps differ from one PDE system to another. On weak interactions, fractal scatterings have been found as well in a weakly discrete sine-Gordon equation and a class of generalized nonlinear Schrödinger (NLS) equations [23, 24, 25]. For these weak interactions, the

[*]Zhou Pei-Yuan Center for Applied Mathematics, Tsinghua University, Beijing 100084, China(zhuyi03@mails.tsinghua.edu.cn).

[†]Department of Mathematics, Southern Methodist University, Dallas, TX 75275,USA(rhaberma@mail.smu.edu)

[‡]Department of Mathematics and Statistics, University of Vermont, 16 Colchester Avenue, Burlington, VT 05401, USA(jyang@cems.uvm.edu)

mathematical analysis can be made more rigorous and quantitative. Indeed, by extending the Karpman-Solovev perturbation method [3], Zhu and Yang derived a simple and asymptotically accurate ODE model for weak interactions in the generalized NLS equations with arbitrary nonlinearities [25]. After various normalizations, this ODE system contains only a single constant parameter which corresponds to different nonlinearities in the PDEs. These ODEs are a two-degrees-of-freedom Hamiltonian system with highly coupled potentials, and their forms are quite different from the collective-coordinate ODE models derived and studied previously for strong interactions [12, 16, 17, 18, 19, 20, 21, 22]. Zhu, Haberman and Yang further analyzed this ODE model and derived a simple second-order map by using asymptotic methods near separatrix orbits [26, 27]. A remarkable feature of this map is that it does not contain any free parameters after various rescalings, thus it is universal for all weak interactions of solitary waves in the generalized NLS equations with arbitrary nonlinearities. Despite its simplicity, this map can capture all the fractal-scattering phenomena of the original PDEs and the reduced ODEs very well both qualitatively and quantitatively [26]. Reduction of weak-interaction dynamics from the PDEs into a simple and universal second-order map is the main contribution of [25, 26, 27]. With the availability of this universal map, one may now expect a complete characterization and understanding of fractal scatterings in weak wave interactions. For instance, we now would like to know under what conditions fractal scatterings would occur or would not occur. For another instance, we now would like to know how these fractals change as nonlinearities of the PDEs and initial conditions of the solitary waves vary. In addition, we now would like to understand how the zoomed-in structures of the fractal are related to the original structures, and how these geometric structures dictate the features of interaction dynamics. All these questions can be answered by a careful analysis of this universal map.

In this paper, we analyze this universal map in detail, which will provide a complete characterization of fractal scatterings in weak wave interactions in the PDEs. First we will show that this map has a fractal structure of its own. We will delineate the map's fractal by tracking its singular curves. Then we will connect the map's fractal to that of the PDE, and thus reach a deep understanding of the PDE's fractal as well as its solution dynamics. In addition, we will determine how the PDE's fractal changes when the soliton parameters and the nonlinearity of the PDE vary. A precise analytical criterion for the occurrence of fractal scatterings in the PDEs will also be given explicitly. All our analytical results are confirmed by direct numerical simulations. These results significantly advance our understanding of fractal scatterings in weak interactions of solitary waves.

2. Previous work. First, we summarize previous relevant work which will form the basis for our later analysis. We consider weak interactions in the generalized NLS equations

$$(2.1) \qquad\qquad iU_t + U_{xx} + N(|U|^2)U = 0.$$

These equations admit solitary waves of the form

$$(2.2) \qquad\qquad U = \Phi(x - \xi)e^{i\phi},$$

where $\Phi(\theta)$ is a localized positive function, $\xi = Vt + x_0$ is the wave's center position, $\phi = V(x - \xi)/2 + (\beta + V^2/4)t - \sigma_0$ is the phase function, and β is the propagation constant (which determines the amplitude of the wave). This wave has four free

parameters: velocity V, amplitude parameter β, initial position x_0, and initial phase constant σ_0. In weak interactions, two such solitary waves are initially well separated with small relative velocities and amplitude differences. Then they would interfere with each other through tail overlapping. When time goes to infinity, they either separate from each other at constant velocities, or form a bound state. The exit velocity, defined as $\Delta V_\infty = |V_2 - V_1||_{t\to\infty}$, depends on the initial conditions of the two waves. When the two waves form a bound state, we define $\Delta V_\infty = 0$. Throughout this paper, we label the left and right waves by numbers 1 and 2 respectively.

In [25], we have shown that for a large class of nonlinearities $N(|U|^2)$, this weak interaction depends on the initial conditions in a sensitive, fractal manner. To analyze this fractal-scattering phenomenon, an extended Karpman-Solov'ev perturbation method was utilized, and the following simple set of dynamical equations for soliton parameters were derived [25]:

$$(2.3) \qquad \begin{aligned} \zeta_{\tau\tau} &= \cos\psi\, e^\zeta, \\ \psi_{\tau\tau} &= (1+\varepsilon)\sin\psi\, e^\zeta. \end{aligned}$$

Here

$$(2.4) \qquad \psi = \Delta\phi, \ \zeta = -\sqrt{\beta}\Delta\xi, \ \tau = \sqrt{\frac{16\beta^{3/2}c^2}{P}}\, t, \ \varepsilon = \frac{P}{2\beta P_\beta} - 1,$$

$\Delta\xi$ and $\Delta\phi$ are the distance and phase difference between the two waves, $\beta = (\beta_{1,0} + \beta_{2,0})/2$, $\beta_{k,0}$ $(k = 1, 2)$ are the initial propagation constants of the two waves, c is the tail coefficient of the solitary wave with propagation constant β, and $P(\beta)$ is the power function of the wave. This ODE system is universal for the PDE (2.1), and different nonlinearities $N(|U|^2)$ only correspond to different constant parameter ε. If $\varepsilon = 0$ [such as when Eq. (2.1) is the original NLS equation], the ODEs (2.3) are integrable, and their solutions have explicit functional expressions [25, 27]. If $\varepsilon \neq 0$, (2.3) is not integrable. In this case, when $\varepsilon > 0$ and under certain initial conditions, we have found that these ODEs exhibit fractal scattering structures which agree with those in the PDEs (2.1) both qualitatively and quantitatively. But when $\varepsilon < 0$, no fractal scatterings arise in these ODEs and their corresponding PDEs under any initial conditions [25].

In order to further understand these fractal scatterings, we have analyzed the ODE system (2.3) extensively in [26, 27] for $|\varepsilon| \ll 1$, using perturbation methods near separatrix orbits. These ODEs are a two-degree-of-freedom Hamiltonian system with the conserved Hamiltonian

$$(2.5) \qquad H(\zeta, \dot\zeta, \psi, \dot\psi) = E + \frac{\varepsilon}{2(1+\varepsilon)}\dot\psi^2,$$

where

$$(2.6) \qquad E = \frac{1}{2}(\dot\zeta^2 - \dot\psi^2) - e^\zeta\cos\psi$$

is called the energy. We also define the momentum M of Eqs. (2.3) as

$$(2.7) \qquad M = \dot\zeta\dot\psi - e^\zeta\sin\psi.$$

Both E and M are conserved when $\varepsilon = 0$, but vary over time when $\varepsilon \neq 0$. If the orbits are escape orbits where $\zeta_\infty \equiv \zeta|_{\tau\to\infty} = -\infty$ (i.e. the two solitary waves eventually

separate from each other after weak interactions), then the exit velocities $|\dot{\zeta}|_\infty$ can be calculated from Eqs. (2.5) and (2.7) as

(2.8)
$$|\dot{\zeta}|_\infty = \sqrt{H + \sqrt{H^2 + M_\infty^2/(1+\varepsilon)}}.$$

In addition, $\dot{\psi}_\infty$, which determines the amplitudes of exiting solitary waves, can also be obtained as $\dot{\psi}_\infty = M_\infty/\dot{\zeta}_\infty$. Thus M_∞ is a key parameter for the prediction of weak-interaction outcomes. In order to calculate M_∞, we notice that for weak wave interactions and when $|\varepsilon| \ll 1$, the ODE solutions [such as $\zeta(\tau)$] oscillate near a sequence of separatrix orbits of the unperturbed ($\varepsilon = 0$) system before they escape to infinity. On these separatrix orbits, $E = M = 0$. If we consecutively enumerate the minimums of $\zeta(\tau)$ (where interactions are the weakest) and denote their energy and momentum values as E_n and M_n (where n is the index of the ζ-minimum), then we can analytically calculate E_n and M_n successively by integrating along the separatrix orbits of the unperturbed system. This was done in [26, 27], and we found that for $|\varepsilon| \ll 1$, E_n does not change, i.e. $E_n = E_0$ for all $n \geq 1$. But M_n does change. In the asymptotic limit of $E_n \ll 1, M_n \ll 1$ and $M_n/E_n \ll 1$, we found that the change of M_n is asymptotically governed by the following second-order separatrix map

(2.9)
$$M_{n+1} = M_n - \mathrm{sgn}(Q_n)\frac{8|E_0|^3\varepsilon}{\pi Q_n^2},$$

(2.10)
$$Q_{n+1} = Q_n + 2M_{n+1},$$

with initial conditions M_0 and Q_0, where $Q_0 = -S_0 M_0$, $S_0 = S|_{\tau=0}$, and

(2.11)
$$S = \frac{2|C|^2\mathrm{Im}(F)}{\pi\mathrm{Re}(C)}, \quad C = \sqrt{\frac{E+iM}{2}}, \quad F = -\frac{1}{C}\mathrm{acoth}(\frac{\dot{\zeta}+i\dot{\psi}}{2C}).$$

Here the multi-valued functions $\sqrt{\cdot}$ and $\mathrm{acoth}(\cdot)$ are chosen uniquely by requiring $\mathrm{Im}(\sqrt{\cdot}) \geq 0$ and $\mathrm{Im}(\mathrm{acoth}(\cdot)) \in [0,\pi)$ at the initial time. The variable Q_n in the above map is an auxiliary variable which is related to the function S.

When the ODEs (2.3) are integrable ($\varepsilon = 0$), S is a conserved quantity. In this case, the integrable solution $\zeta(\tau)$ develops finite-time singularity if $S_0 = 2k, \mathrm{Re}(C_0) \neq 0, k = 0, \pm1, \pm2, ...$, or $\mathrm{Re}(C_0) = 0, \mathrm{Im}(F_0) = 0$, see [27] for details. These finite-time singularities play important roles in the formation of fractal scatterings. Indeed, it was observed from numerical simulations in [25] that fractal structures for $\varepsilon \neq 0$ bifurcate out from points where integrable solutions develop finite-time singularities. This fact will be proved in this paper by the analysis of the map.

The map (2.9)-(2.10) can be normalized into a very simple form. Let

(2.12)
$$G = \frac{8|E_0|^3\varepsilon}{\pi}, \quad m_n = G^{-1/3}M_n, \quad q_n = G^{-1/3}Q_n,$$

then this map becomes

(2.13)
$$m_{n+1} = m_n - \frac{\mathrm{sgn}(\varepsilon q_n)}{q_n^2},$$

(2.14)
$$q_{n+1} = q_n + 2m_{n+1}.$$

This normalized map is second-order, and it does not contain any free parameters (except a sign of ε). Thus it is universal for all weak two-wave interactions in the generalized NLS equations (2.1) with arbitrary nonlinearities. For positive and negative

signs of ε, we will show this map has completely different behaviors. This explains why fractal scatterings appear in ODEs (2.3) only when $\varepsilon > 0$, but not when $\varepsilon < 0$. Details will be given in Secs. 4 and 6.

To demonstrate the validity and accuracy of the above simple separatrix map for describing fractal scatterings in the original PDEs (2.1), here we compare the fractal scattering structures obtained from the PDEs (2.1), the ODEs (2.3), and the map (2.13)-(2.14). In all our comparisons below and in later sections, we take the cubic-quintic nonlinearity

$$(2.15) \qquad N(|U|^2) = |U|^2 + \delta|U|^4$$

with $\delta = 0.0003$ in the PDE (2.1) (comparisons with other forms of nonlinearities are similar, see [25]). We take two types of initial conditions for the two solitary waves in the PDE (2.1). One is that

$$(2.16) \qquad \beta_{0,1} = \beta_{0,2} = 1,$$

where the two waves initially have the same amplitudes. The other one is that

$$(2.17) \qquad \beta_{0,1} = 1.0325, \quad \beta_{0,2} = 0.9675,$$

where the two waves initially have unequal amplitudes. In both cases, the other parameters in the two initial solitary waves are the same as

$$(2.18) \qquad x_{0,2} = -x_{0,1} = 5, \quad V_{0,1} = V_{0,2} = 0, \quad \phi_{0,1} = 0.$$

That is, the two waves initially have equal velocities and are separated by 10 spatial units. The initial phase of the first wave $\phi_{0,1}$ can always be set as zero by phase invariance of the PDE (2.1), thus it does not constitute a restriction on the initial conditions. For both types of initial conditions, $\Delta\phi_0(= \phi_{0,2})$ is used as the control parameter. Corresponding to both types of initial conditions, we find from Eq. (2.4) that $\varepsilon = 0.001$ in the ODEs (2.3).

For the first type of initial conditions (2.16), the corresponding initial conditions of the ODEs are

$$(2.19) \qquad \zeta_0 = -10, \quad \dot{\zeta}_0 = \dot{\psi}_0 = 0,$$

and $\psi_0(= \phi_{0,2})$ is the control parameter. For the map (2.13)-(2.14), the corresponding initial conditions can be readily found to be

$$(2.20) \qquad q_0 = m_0 = -\frac{1}{2}\pi^{1/3}\tan\psi_0 \cdot \varepsilon^{-1/3}$$

since $S_0 = -1$ in view of the expression (2.11) for S. Here we have assumed $\cos\phi_0 > 0$ since we have shown before [27] that fractal scatterings arise only in this case.

For the second type of initial conditions (2.17), the corresponding initial conditions of the ODEs are

$$(2.21) \qquad \zeta_0 = -10, \quad \dot{\zeta}_0 = 0, \quad \dot{\psi}_0 = -0.01167.$$

The corresponding initial conditions of the map are

$$(2.22) \qquad m_0 = T(\psi_0)\varepsilon^{-1/3}, \qquad q_0 = -T(\psi_0)S(\psi_0)\varepsilon^{-1/3},$$

where

$$(2.23) \qquad T(\psi_0) = \frac{-\pi^{1/3} \sin \psi_0}{2 \cos \psi_0 + \dot{\psi}_0^2 e^{-\zeta_0}},$$

and $S(\psi_0)$ is defined in (2.11).

For each of the above two types of initial conditions, we have simulated the PDE (2.1), the ODEs (2.3), and the map (2.13)-(2.14) for various values of the control parameter $\Delta\phi_0$, and obtained the corresponding exit velocities ΔV_∞ [in the case of the ODEs and the map, the exit velocities have been obtained and properly rescaled through the formula (2.8) and relations (2.4), (2.12)]. In all cases, we observed fractal scattering phenomena. For the first type of initial conditions (2.16) (where the two waves initially have equal amplitudes), the fractal structures from the PDE, ODE and the map are displayed in Fig. 2.1. Here the fractals are symmetric in $\Delta\phi_0$, and they lie in a narrow interval near the $\Delta\phi_0 = 0$ point (only a segment of the parameter region is shown for better visualization). We see that the three structures match very well both qualitatively and quantitatively. For the second type of initial conditions (2.17) (where the two waves initially have un-equal amplitudes), the fractal structures from the PDE, ODE and the map are displayed in Fig.2.2. Here the fractals lie in a wide interval of $\Delta\phi_0 \in [0, \pi]$, and they do not possess any symmetry. Again these structures match very well. These comparisons show that the intricate fractal scatterings in the PDEs (2.1) and the ODEs (2.3) CAN be accurately predicted by the simple map (2.13)-(2.14). These are the main results which have been obtained before in [25, 26, 27].

In order to reach a complete understanding and characterization of these fractal structures and their solution dynamics in weak wave interactions, the separatrix map (2.13)-(2.14) needs to be carefully analyzed. This map exhibits a fractal structure of its own in its initial-condition space (when $\text{sgn}(\varepsilon) = 1$) [26]. If this fractal of the map is well understood, then through connections of variables between the map and the PDEs/ODEs, the fractals in the PDEs/ODEs will be well characterized. In the following sections, we will analyze this map and use this information to delineate weak-interaction dynamics in the PDEs/ODEs.

3. Analysis of the fractal in the separatrix map. The separatrix map (2.13)-(2.14) depends only on the sign of ε, which can be 1 or -1. It turns out that this map has completely different dynamics for $\text{sgn}(\varepsilon) = 1$ and -1. When $\text{sgn}(\varepsilon) = 1$, this map is fractal-bearing, while when $\text{sgn}(\varepsilon) = -1$, it is not [26]. This is consistent with the numerical observation of [25] that fractal scatterings occur in the ODEs (2.3) only when $\varepsilon > 0$ but not when $\varepsilon < 0$. In this section, we analyze the fractal in this map when $\text{sgn}(\varepsilon) = 1$.

For convenience, we rewrite the map (2.13)-(2.14) as

$$(3.1) \qquad \begin{pmatrix} q_{n+1} \\ m_{n+1} \end{pmatrix} = \mathcal{F} \begin{pmatrix} q_n \\ m_n \end{pmatrix},$$

where

$$(3.2) \qquad \mathcal{F} \begin{pmatrix} q \\ m \end{pmatrix} = \begin{pmatrix} q + 2m - \frac{2sgn(q)}{q^2} \\ m - \frac{sgn(q)}{q^2} \end{pmatrix}.$$

It can be seen that $\mathcal{F}$ is differentiable when $q \neq 0$. The Jacobian of $\mathcal{F}$ is

$$(3.3) \qquad J_{\mathcal{F}} = \begin{pmatrix} 1 + 4\frac{sgn(q)}{q^3} & 2 \\ 2\frac{sgn(q)}{q^3} & 1 \end{pmatrix}.$$
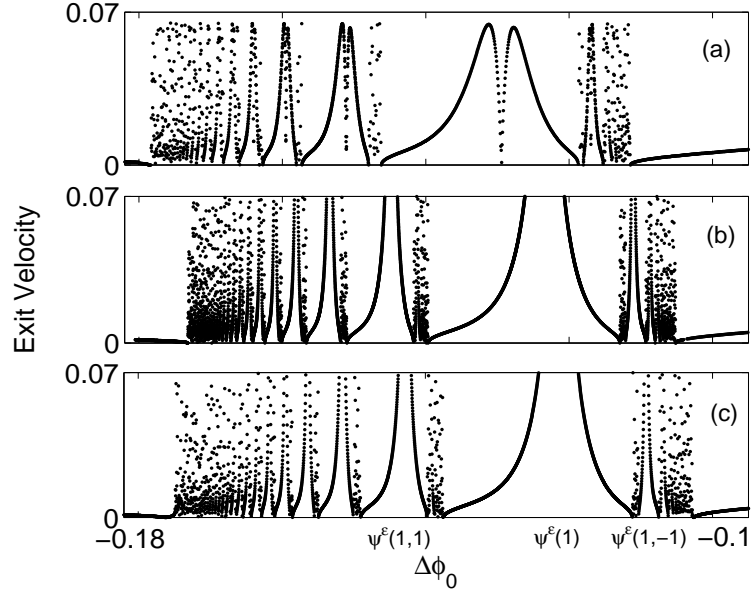
FIG. 2.1. *Comparisons of exit-velocity fractals from (a) PDE simulations, (b) ODE predictions, and (c) map predictions for the equal-amplitude initial conditions (2.16). The marked segment in (b) is amplified in Fig. 5.1, where the solution dynamics in this segment is also shown. Labels $\psi^\varepsilon(1), \psi^\varepsilon(1,1), \ldots$ are locations of singularity peaks (of infinite height) in (c), which correspond to intersections of the initial-value curve λ^ε with the map's singular curves $\gamma(1), \gamma(1,1), \ldots$ in Fig. 4.1 (see Sec. 4.1 for details).*
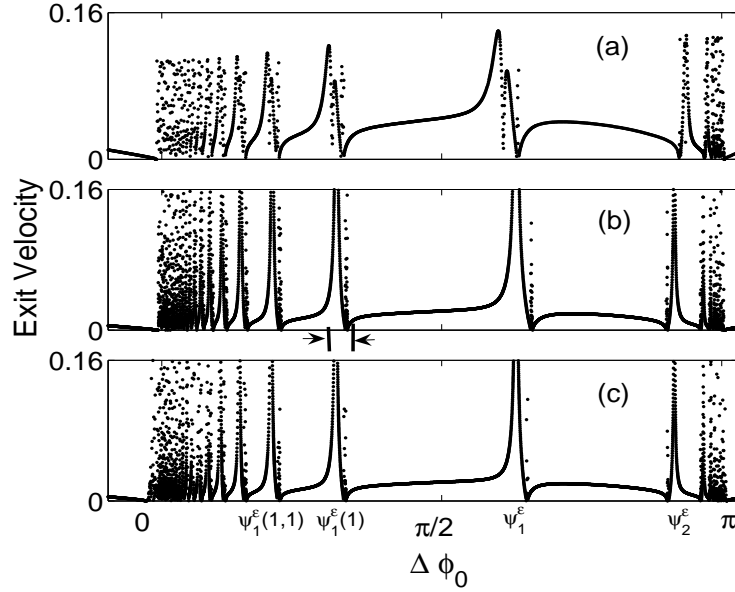

FIG. 2.2. *Comparisons of exit-velocity fractals from (a) PDE simulations, (b) ODE predictions, and (c) map predictions for the unequal-amplitude initial conditions (2.17). For the segment of structures marked in (b), its movement with varying values of ε is displayed in Fig. 4.4. Labels $\psi_1^\varepsilon, \psi_1^\varepsilon(1), \ldots$ are locations of singularity peaks in (c) which correspond to intersections of the initial-value curve λ^ε with the map's singular curves $\gamma_0, \gamma(1), \ldots$ in Fig. 4.3 (see Sec. 4.2 for details).*

The determinant of this Jacobian matrix is equal to one, thus the map $\mathcal{F}$ is area-preserving and orientation-preserving. Chaos if it occurs will be Hamiltonian chaos [29].

It is easy to see that $\mathcal{F}^n(-q, -m) = -\mathcal{F}^n(q, m)$, thus $\mathcal{F}^n$ is anti-symmetric with respect to the origin. It can also be seen that $\mathcal{F}$ does not have any (bounded) fixed points, but it has a lot of periodic orbits. For example, $\{(2^{-1/3}, 2^{-1/3}), (-2^{-1/3}, -2^{-1/3})\}$ is a period-2 orbit, and $\{(1,1), (1,0), (-1,-1), (-1,0)\}$ is a period-4 orbit. One can easily verify that these two periodic orbits are both unstable. All the other periodic orbits are unstable too as we will see later in this section.

An important property of the map $\mathcal{F}$ is that it is reversible in $\mathbb{R}^2 \backslash \Omega$, where $\mathbb{R}$ is the set of real numbers, and

$$\Omega = \{(q, m) \in \mathbb{R}^2 : q = 2m\}.$$

Indeed, $\mathcal{F}^{-1}$ has an explicit formula when $q \neq 2m$:

$$(3.4) \qquad \mathcal{F}^{-1} \left(\begin{array}{c} q \\ m \end{array} \right) = \left(\begin{array}{c} q - 2m \\ m + \frac{sgn(q-2m)}{(q-2m)^2} \end{array} \right).$$

In the later text, we will utilize two subsets of the (q, m) plane which we define here:

$$\Omega^+ = \{(q, m) \in \mathbb{R}^2 : q - 2m > 0\},$$

and

$$\Omega^- = \{(q, m) \in \mathbb{R}^2 : q - 2m < 0\}.$$

3.1. Singular curves of the map and their identifications. The limit behaviors $\lim_{n \to \infty} \mathcal{F}^n(q_0, m_0)$ are important as they correspond to the outcomes of weak interactions. Indeed, from $m_\infty = \lim_{n \to \infty} m_n$ and the scaling relations (2.12), we can obtain the exit velocities $|\dot{\zeta}_\infty|$ from Eq. (2.8). For almost all initial points (q_0, m_0), m_∞ exists and is finite (while $q_\infty = \pm\infty$). Thus orbits of almost all initial points eventually escape to $q_\infty = \infty$ or $-\infty$ along the horizontal (constant-m) direction. But there are two special sets of initial points which are different. One set is the initial points which make $q_n = 0$ for some $n \geq 0$, i.e.

$$(3.5) \qquad \mathcal{S} = \{(q_0, m_0) \in \mathbb{R}^2 : q_n = 0, \, n = 0, 1, 2, ...\}.$$

For these points, iterations can not continue for (q_{n+1}, m_{n+1}) since $q_n = 0$, thus we call them singular points, and $\mathcal{S}$ the singular set. On these points, we formally let $m_{n+1} = \infty$, and consequently $m_\infty = \infty$ as well. For singular initial points, the exit velocities of weak interactions are infinite [see Eq. (2.8)], thus they correspond to peaks (of infinite height) in Fig. 2.1(c). The other set is the initial points (q_0, m_0) which are periodic or quasi-periodic. On these points, m_n oscillates forever, hence m_∞ does not exist. These points correspond to spatially-localized and temporally oscillating bound states in the PDEs (2.1). In this case, we set $m_\infty = 0$, which gives zero separation velocities $|\dot{\zeta}_\infty|$ from Eq. (2.8) (recall that $H < 0$ for fractal scatterings [27]). This way, m_∞ can be defined everywhere in the initial value plane (q_0, m_0). Numerically we have computed $|m_\infty|$ over this plane (iterating 500 steps instead of infinite steps), and the result is plotted in Fig. 3.1 (here color levels correspond to $|m_\infty|$ values). This graph is a fractal, as can be easily verified by repeated zooms into it.
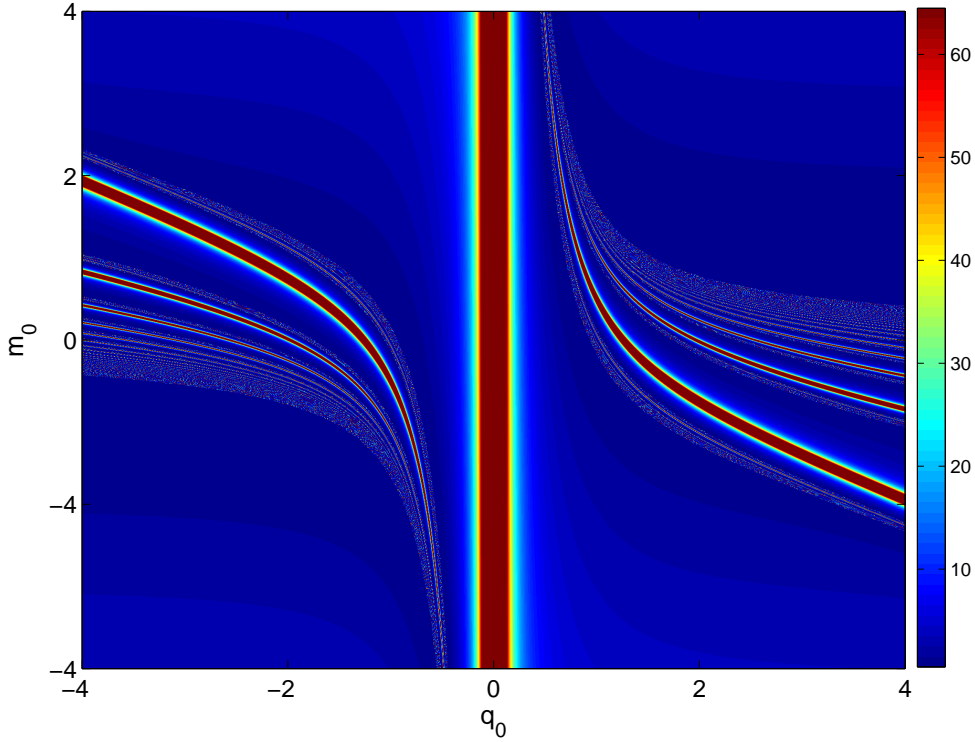
FIG. 3.1. *Values of $|m_\infty|$ in the initial-value space (q_0, m_0) for the map (2.13)-(2.14) with $sgn(\varepsilon) = 1$. Colors represent value levels of $|m_\infty|$.*

In Fig. 3.1, singular points form an infinite number of smooth curves. Each of these singular curves lies in the middle of a red stripe (of varying thickness), and all these singular curves form the backbone of the map's fractal in Fig. 3.1. These singular curves are directly related to the singularity peaks (of infinite height) in the map's exit-velocity fractals in Figs. 2.1(c) and 2.2(c). This is because on a singular curve, $m_\infty = \infty$, thus the corresponding exit velocity is also infinite [see Eq. (2.8)]. In view of this, these singular curves correspond to the singularity peaks in the ODE's exit-velocity fractals and counterpart structures in the PDE's exit-velocity fractals. These singularity peaks (or their counterparts) in turn form the backbones of the map's, ODE's and PDE's exit-velocity fractals in Figs. 2.1 and 2.2. Thus if we can clearly characterize the singular curves of the map, then a good understanding of the fractals in the ODEs and PDEs will be reached. In the rest of this section, we focus on these singular curves. We will determine where they are located, how to identify them, what dynamics they represent, and what their asymptotics are at large or small values of q_0.

About these singular curves, each one is characterized by a unique finite binary sequence $\mathbf{a} = \text{sgn}(q_0, q_1, ..., q_n)$. Singular points on the same curve have the same binary sequence, while different singular curves have different sequences. Let us denote the singular curve with a binary sequence $\mathbf{a} = (a_0, a_1, ..., a_n)$ as $\gamma(\mathbf{a})$. Then

$$(3.6) \qquad \gamma(\mathbf{a}) = \{(q_0, m_0) \in \mathbb{R}^2 : \ q_{n+1} = 0, \ \text{sgn}(q_0, q_1, ..., q_n) = \mathbf{a}\}.$$
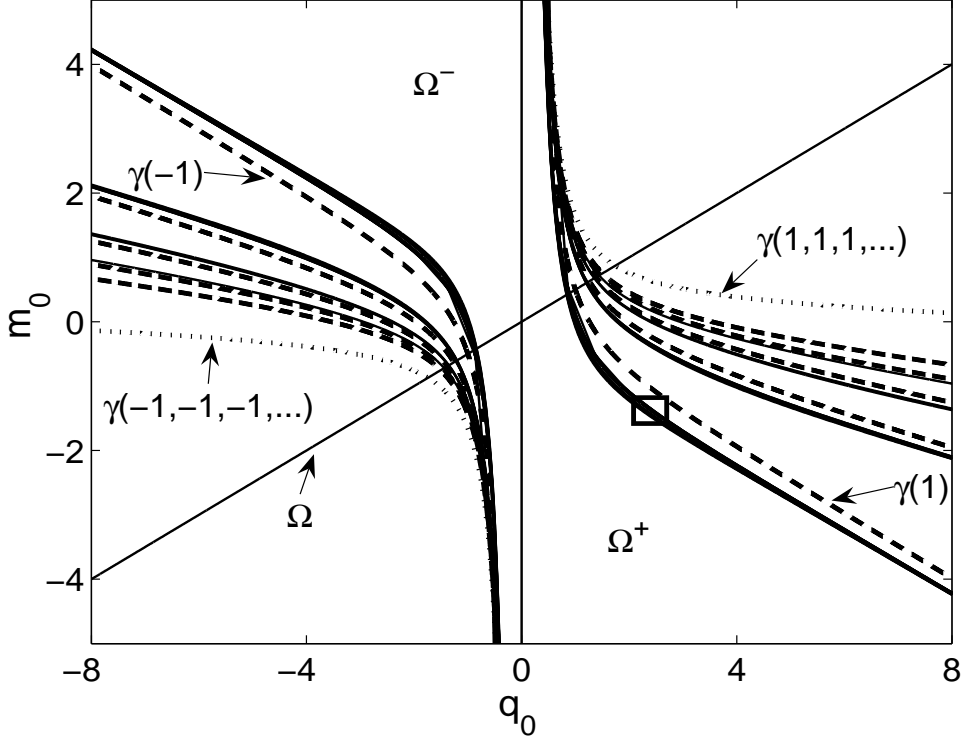
FIG. 3.2.   *Plots of singular curves* $\gamma(a_0), \gamma(a_0, a_1), \gamma(a_0, a_1, a_2),$ $\gamma(a_0, a_1, a_2, a_3),$ *and* $\gamma(a_0, a_1, a_2, a_3, a_4)$ *for all binary numbers of* $a_0, \ldots, a_4$. *The dashed lines in the right plane are* $\gamma(1),$ $\gamma(1,1),$ $\gamma(1,1,1),$ $\gamma(1,1,1,1)$ *and* $\gamma(1,1,1,1,1)$ *respectively from left to right. The accumulation curve* $\gamma(1,1,1,\ldots)$ *is also shown (as dotted lines). Lines in the left half plane are similar. The box region will be magnified in Fig.3.3.*

Here we allow **a** to be empty, in which case we get the simplest singular curve

$$(3.7) \qquad\qquad \gamma_0 = \{(q_0, m_0) : q_0 = 0\},$$

which is the vertical axis. When $n = 0$ (where $q_1 = 0$), we see from the map (3.2) that

$$(3.8) \qquad\qquad \gamma(1) = \{(q_0, m_0) : m_0 = -q_0/2 + 1/q_0^2, \ q_0 > 0\},$$
$$(3.9) \qquad\qquad \gamma(-1) = \{(q_0, m_0) : m_0 = -q_0/2 - 1/q_0^2, \ q_0 < 0\}.$$

These two curves are plotted in Fig. 3.2. They are located in the middle of the thickest red stripes in the right and left half planes of Fig. 3.1.

Now we determine the relations between singular curves with different binary sequences. From our definitions, we see that if $(q_0, m_0) \in \gamma(a_0, \mathbf{a})$, then $\mathcal{F}(q_0, m_0) \in \gamma(\mathbf{a})$, where $\mathbf{a}$ is any finite binary sequence and $a_0 = \pm 1$. In addition, if $a_0 = 1$, i.e. $q_0 > 0$, then $q_1 - 2m_1 > 0$ in view of Eq. (2.14), thus $\mathcal{F}(q_0, m_0) \in \Omega^+$. Similarly if $a_0 = -1$, then $\mathcal{F}(q_0, m_0) \in \Omega^-$. As a result, we have

$$(3.10) \qquad\qquad \mathcal{F}(\gamma(1, \mathbf{a})) = \gamma(\mathbf{a}) \bigcap \Omega^+,$$
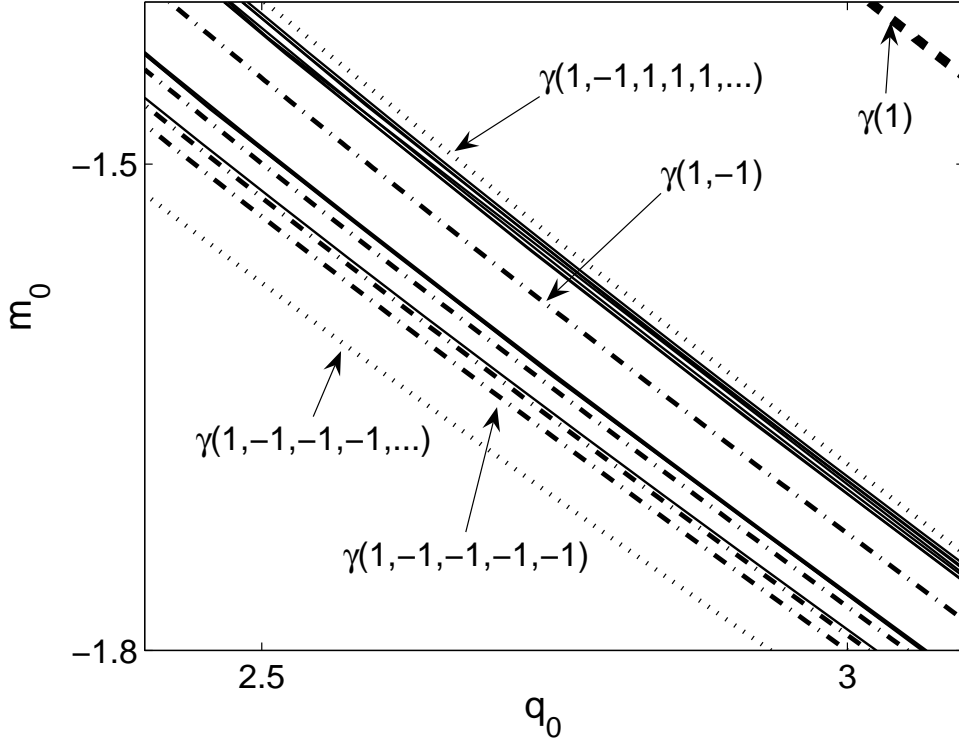$$(3.11) \qquad\qquad \mathcal{F}(\gamma(-1, \mathbf{a})) = \gamma(\mathbf{a}) \bigcap \Omega^-.$$

FIG. 3.3. *Amplification of the box region in Fig. 3.2. The dash-doted lines are $\gamma(1,-1)$, $\gamma(1,-1,-1)$, $\gamma(1,-1,-1,-1)$ and $\gamma(1,-1,-1,-1,-1)$ respectively from right to left. Accumulation curves $\gamma(1,-1,-1,-1,\ldots)$ and $\gamma(1,-1,1,1,1,\ldots)$ are also shown.*

Or written differently, we have

$$\gamma(1,\mathbf{a}) = \mathcal{F}^{-1}(\gamma(\mathbf{a})\bigcap \Omega^+), \tag{3.12}$$

$$\gamma(-1,\mathbf{a}) = \mathcal{F}^{-1}(\gamma(\mathbf{a})\bigcap \Omega^-). \tag{3.13}$$

These relations tell us that each singular curve $\gamma(\mathbf{a})$ has two pre-image singular curves $\gamma(1,\mathbf{a})$ and $\gamma(-1,\mathbf{a})$ under the map $\mathcal{F}$. In particular, $\gamma(1)$ and $\gamma(-1)$ are the two pre-image singular curves of γ_0.

Thus from the basic singular curve γ_0 given in Eq. (3.7), two singular curves $\gamma(1)$ and $\gamma(-1)$ in Eqs. (3.8)-(3.9) are obtained. We can successively construct $\gamma(\mathbf{a})$ for any finite binary sequence $\mathbf{a}$ by repeatedly applying the inverse map $\mathcal{F}^{-1}$ on γ_0. The first few of these singular curves are plotted in Fig. 3.2. It is easy to see from the map (3.2) that for any binary sequence $\mathbf{a}$, $\gamma(\mathbf{a})$ and $\gamma(-\mathbf{a})$ are anti-symmetric to each other about the origin, i.e.

$$\gamma(-\mathbf{a}) = -\gamma(\mathbf{a}), \tag{3.14}$$

thus we only consider curves on the right half plane with $\mathbf{a} = (1, a_1, ..., a_n)$ below. From Fig. 3.2, we see that $\gamma(1)$, $\gamma(1,1)$, $\gamma(1,1,1)$, ... form the primary cascading sequence from the left to the right. This sequence accumulates to the limit curve $\gamma(1,1,1,1,...)$ which is plotted as a dotted line in Fig. 3.2 and can be seen in Fig.

3.1. This primary sequence of singular curves defines the overall geometry of the map's fractal in Fig. 3.1. On the left side of each primary curve, there is a secondary structure whose infinite curves are very close to each other and thus visually show as one "thick curve" in Fig. 3.2. Each secondary structure lies near its corresponding primary curve. To probe these secondary structures, we zoom into the box region of Fig. 3.2, which contains a segment of the secondary structure for the primary curve $\gamma(1)$. The result is shown in Fig. 3.3. From this zoomed-in graph, we see that among numerous curves in this secondary structure, there is a secondary sequence of curves $\gamma(1,-1)$, $\gamma(1,-1,-1)$, $\gamma(1,-1,-1,-1)$,... which cascades to the left. This secondary curve sequence defines the overall geometry of this secondary structure. Near each curve in this secondary sequence (and on its right hand side), there is a higher-order structure which can be probed by repeated zooms. Every time one zooms into a higher-order structure, the cascading direction of its higher-order sequence is reversed, and the side of the higher-order sequence relative to its associated curve (either left or right) is also reversed. The binary sequences for these higher-order-sequence curves are $\{(\mathbf{a},1), (\mathbf{a},1,1), (\mathbf{a},1,1,1), ...\}$ when the sequence cascades to the right and lies on the right side of $\gamma(\mathbf{a})$, and $\{(\mathbf{a},-1), (\mathbf{a},-1,-1), (\mathbf{a},-1,-1,-1) ...\}$ when the sequence cascades to the left and lies on the left side of $\gamma(\mathbf{a})$. Here $\mathbf{a}$ is the binary sequence for the associated curve of this higher-order sequence.

Based on the above pattern, we can identify any singular curve with an arbitrary binary sequence. For instance, to identify the curve with a binary sequence $\mathbf{a} = (1,1,-1,-1,-1,1,-1)$, we first go to the curve $\gamma(1)$ (see Fig. 3.2), find its associated primary sequence (which lies on its right hand side), and pick out the first member of that sequence (not counting $\gamma(1)$ itself). The picked curve is then $\gamma(1,1)$, see Fig. 3.2. Next, we go to the secondary curve sequence of $\gamma(1,1)$ (which lies on its left) and pick out the third member of that sequence, which is $\gamma(1,1,-1,-1,-1)$. Next we go to the higher-order sequence of $\gamma(1,1,-1,-1,-1)$ (which lies on its right) and pick out the first member of that sequence, which is $\gamma(1,1,-1,-1,-1,1)$. Lastly we go to the higher-order sequence of $\gamma(1,1,-1,-1,-1,1)$ (which lies on its left) and pick out the first member of that sequence, which will be the singular curve $\gamma(1,1,-1,-1,-1,1,-1)$ that we are looking for.

We have noted earlier in this section that the map $\mathcal{F}$ has a lot of periodic orbits. Then an interesting question is where these periodic orbits are located in the map's fractal in Fig. 3.1, and how these orbits are related to the above singular curves. Clearly every periodic point can not lie on a singular curve $\gamma(\mathbf{a})$ with a finite binary sequence $\mathbf{a}$ in view of the definition (3.6) of $\gamma(\mathbf{a})$. But a periodic point can be viewed as being on a singular curve with an infinite binary sequence $\mathbf{a}$ whose digits are the signs of q of the successive iteration points which repeat with the same period as the periodic point (here a singular curve with an infinite binary sequence can be defined as the limit of the singular curve with a finite binary sequence). Using this viewpoint, we can understand where periodic points should be located in the map's fractal. For instance, in the period-two orbit $\{(2^{-1/3},2^{-1/3}), (-2^{-1/3},-2^{-1/3})\}$, the first point $(2^{-1/3},2^{-1/3})$ lies on the singular curve with the binary sequence $\mathbf{a} = (1,-1,1,-1,\ldots)$, while the second point $(-2^{-1/3},-2^{-1/3})$ lies on the singular curve with the binary sequence $\mathbf{a} = (-1,1,-1,1,\ldots)$. For another instance, in the period-four orbit $\{(1,1),(1,0),(-1,-1),(-1,0)\}$, the point $(1,1)$ lies on the singular curve with a binary sequence $(1,1,-1,-1,1,1,-1,-1,\ldots)$, and the point $(1,0)$ lies on the singular curve with a binary sequence $(1,-1,-1,1,1,-1,-1,1,\ldots)$, etc. The singular curves with these infinite binary sequences can be identified by the same scheme as

we detailed above, thus we can ascertain where these periodic points are located in the map's fractal. Obviously these infinite binary sequences of periodic points are infinitely close to their finite truncations, and points on the singular curves with truncated finite binary sequences have very different trajectories from those of the periodic points. Thus the periodic points of the map $\mathcal{F}$ are all unstable.

From the above singular-curve identification scheme, we see that all the singular curves on the right half of the (q_0, m_0) plane lie between two special accumulation curves, $\gamma(1, 1, 1, 1, ...)$ and $\gamma(1, -1, -1, -1, -1, ...)$ (see Figs. 3.2 and 3.3). So does the fractal of the map on the right half plane as well (see Fig. 3.1). In the whole plane, the map's fractal lies between the two accumulation curves $\gamma(1, 1, 1, \ldots)$ and $\gamma(-1, -1, -1, \ldots)$.

Similar to the above tracking and identification of singular curves, we can also track how regions in the (q, m) plane move under the map $\mathcal{F}$. This is helpful for us to see how the orbit of an initial point moves in the (q, m) plane. Let us denote the regions above $\gamma(1, 1, 1, \ldots)$ and below $\gamma(-1, -1, -1, \ldots)$ as $\mathcal{D}_0$, and the region between $\gamma(1, -1, -1, -1, \ldots)$ and $\gamma(-1, 1, 1, 1, \ldots)$ as $\mathcal{D}_1$. Then we find that

$$(3.15) \qquad\qquad \mathcal{F}^{-1}(\mathcal{D}_0) = \mathcal{D}_0 \cup \mathcal{D}_1.$$

Other regions such as $\mathcal{F}^{-1}(\mathcal{D}_1)$ can be obtained with the help of singular curves whose pre-images under the inverse map $\mathcal{F}^{-1}$ have been detailed above (notice that the singular curve γ_0 lies in the middle of the region $\mathcal{D}_1$). Details will not be pursued in this paper.

3.2. Asymptotic behaviors of singular curves. Next we determine the asymptotic behaviors of singular curves as $q_0 \to 0$ and $\pm\infty$. These asymptotic behaviors will be needed for our derivation of scaling laws of the exit-velocity fractals in the ODEs and PDEs as $\varepsilon \to 0$ under the unequal-amplitude initial conditions (2.17), see Sec. 4.2. But they will not be needed for scaling laws of fractals with equal-amplitude initial conditions (2.16), see Sec. 4.1. Since $\gamma(\mathbf{a})$ and $\gamma(-\mathbf{a})$ are anti-symmetric to each other, we only consider curves on the right half plane with $\mathbf{a} = (1, a_1, ..., a_n)$ below.

The asymptotic behaviors of singular curves $\gamma(1, a_1, ..., a_n)$ as $q_0 \to 0^+$ and $+\infty$ can be obtained from $\gamma(1)$ in Eq. (3.8) and the recursion relations (3.12)-(3.13), and we get the following results:

1. For any singular curve $\gamma(1, \mathbf{a})$, if $(q_0, m_0) \in \gamma(1, \mathbf{a})$, then

$$(3.16) \qquad\qquad m_0 = q_0^{-2} + C_{\mathbf{a}} + ..., \quad q_0 \to 0^+,$$

   where $(2C_{\mathbf{a}}, C_{\mathbf{a}})$ is the intersection point between $\gamma(\mathbf{a})$ and Ω.

2. If $(q_0, m_0) \in \gamma(1, a_1, ..., a_n)$ with $a_1 = ... = a_n = 1$ (i.e. on a primary singular curve), then

$$(3.17) \qquad\qquad m_0 = -\frac{1}{2(n+1)} q_0 + D_n q_0^{-2} + ..., \quad q_0 \to +\infty,$$

   where

$$(3.18) \qquad\qquad D_n = 1 + \frac{n+1}{n} D_{n-1}, \quad D_0 = 1.$$

3. If $(q_0, m_0) \in \gamma(1, a_1, ..., a_n, -1, \hat{\mathbf{a}})$ where $a_1 = ... = a_n = 1$ and $\hat{\mathbf{a}}$ is an arbitrary finite binary sequence, i.e. when (q_0, m_0) lies in the secondary

structure of a primary curve $\gamma(1, a_1, ..., a_n)$, then

$$
\begin{aligned}
m_0 = \quad & -\frac{1}{2(n+1)} q_0 - \frac{1}{\sqrt{2(n+1)}} q_0^{-1/2} \\
& + \frac{(n+1)C_{\hat{\mathbf{a}}}}{\sqrt{2}} q_0^{-3/2} + ..., \quad q_0 \to +\infty.
\end{aligned}
$$
(3.19)

where $(2C_{\hat{\mathbf{a}}}, C_{\hat{\mathbf{a}}})$ is the intersection point between $\gamma(\hat{\mathbf{a}})$ and Ω.

Notice from (3.17) and (3.19) that for any binary subsequence $\hat{\mathbf{a}}$, $\gamma(1, a_1, .., a_n, -1, \hat{\mathbf{a}})$ tends to $\gamma(1, a_1, ..., a_n)$ as $q_0 \to +\infty$, i.e. the distance between them goes to zero at large q_0 values. This explains why we could (and should) treat singular curves $\gamma(1, \mathbf{a}, -1, \hat{\mathbf{a}})$ with arbitrary binary subsequences $\hat{\mathbf{a}}$ as the secondary structures associated with the primary curve $\gamma(1, \mathbf{a})$ earlier in this section.

To prove the first asymptotic result (3.16), let

$$
(3.20) \qquad (q_0, m_0) = \mathcal{F}^{-1}(q_1, m_1) = (q_1 - 2m_1, m_1 + \frac{\operatorname{sgn}(q_1 - 2m_1)}{(q_1 - 2m_1)^2}).
$$

Then using (2.14), we get

$$
(3.21) \qquad\qquad m_0 = \frac{q_1}{2} - \frac{q_0}{2} + \frac{\operatorname{sgn}(q_0)}{q_0^2}.
$$

For $(q_0, m_0) \in \gamma(1, \mathbf{a})$, in view of the recursion relation (3.12), we see that $(q_1, m_1) \in \gamma(\mathbf{a}) \bigcap \Omega^+$. When $q_0 \to 0^+$, (3.20) shows that $q_1 - 2m_1 \to 0^+$. Thus (q_1, m_1) approaches the intersection point between $\gamma(\mathbf{a})$ and Ω, i.e. $q_1 \to 2C_{\mathbf{a}}$ and $m_1 \to C_{\mathbf{a}}$. Substituting these asymptotic results into (3.21), (3.16) is then obtained.

The second and third asymptotic relations (3.17) and (3.19) can be proved by the induction method and by utilizing the recursion relation (3.12). These proofs are elementary and will be omitted.

4. Scaling properties of fractals in the ODEs and PDEs. We have known that fractal structures in the ODEs (2.3) and PDEs (2.1) are completely determined by the map's fractal, together with the initial-value connections (2.4) and variable scalings (2.12) between the map and the ODEs/PDEs. Utilizing the knowledge we have gained on the map's fractal in the previous section, we can now obtain a deep understanding on the fractals in the ODEs and the PDEs. This will be demonstrated in this section. For definiteness, we will use the two types of initial conditions (2.16) and (2.17) as examples. In both cases, as the initial phase difference ψ_0 changes, the corresponding initial condition of the map forms a parameterized curve in the (q_0, m_0) plane. This curve, denoted as λ^ε, intersects the map's $|m_\infty|$ fractal in Fig. 3.1, and this intersection then completely determines the exit-velocity fractals of the ODEs and PDEs shown in Figs. 2.1 and 2.2.

4.1. The case of equal-amplitude initial conditions. In this subsection, we consider the first type of initial conditions (2.16) where the two solitary waves initially have equal amplitudes. In this case, the corresponding curve of the map's initial points in the (q_0, m_0) plane can be seen from (2.20) as

$$
(4.1) \qquad \lambda^\varepsilon = \{(q_0, m_0) : q_0 = m_0 = -\frac{\pi^{1/3}}{2\varepsilon^{1/3}} \tan \psi_0, \ \psi_0 \in (-\pi/2, \pi/2)\}.
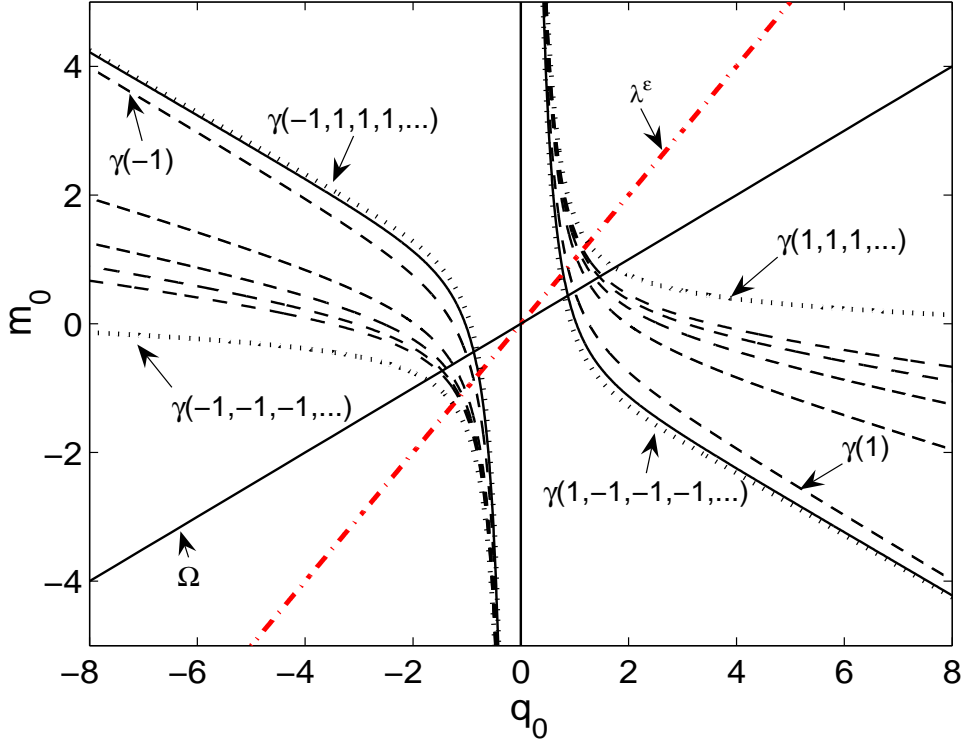$$

FIG. 4.1. *Curve λ^ϵ of the map's initial points (4.1) which corresponds to the equal-amplitude initial conditions (2.16). Some singular curves are also shown. The dashed curves are the same as those in Fig. 3.2, and the solid curves are $\gamma(1, -1)$ and $\gamma(-1, 1)$.*

The reason for the restriction $\psi_0 \in (-\pi/2, \pi/2)$ is that fractal scatterings can only arise in the ψ_0 intervals where $H < 0$ [27]. In the present case, $H < 0$ corresponds to the interval $\psi_0 \in (-\pi/2, \pi/2)$. This parameterized curve λ^ε is a straight line with slope one in the (q_0, m_0) plane, see Fig. 4.1.

The map's $|m_\infty|$ fractal in the initial-condition plane (q_0, m_0) (see the previous section) is very instrumental for the understanding of exit-velocity fractals in the PDEs and ODEs. First of all, from the map's $|m_\infty|$ fractal, together with the initial-value curve (4.1), the formula (2.8) and various scalings, we can easily construct the map's exit-velocity fractal in Fig. 2.1(c). This exit-velocity fractal of the map can be readily understood. For instance, let us denote the ψ_0 value at the intersection of λ^ε with a singular curve $\gamma(\mathbf{a})$ as $\psi^\varepsilon(\mathbf{a})$. At each $\psi^\varepsilon(\mathbf{a})$, the map's exit-velocity graph has a singularity peak of infinite height. To illustrate, a few simple $\psi^\varepsilon(\mathbf{a})$ values are marked in Fig. 2.1(c). Using this connection, the map's exit-velocity graph can be completely understood from the map's $|m_\infty|$ fractal. Then the exit-velocity fractals in the ODEs and PDEs can be similarly understood. To be specific, we find that the primary window sequence in the exit-velocity fractals of Fig. 2.1, which cascades to the left with the first member being the widest window, are associated with the primary sequence of singular curves $\{\gamma(1), \gamma(1, 1), \ldots\}$ (at the intersection with the set λ^ε). The dense secondary structure on the right hand side of each primary window in the exit-velocity fractals of Fig. 2.1 corresponds to the secondary structure of each primary-sequence curve in the map's $|m_\infty|$ fractal. In particular, the value $\psi^\varepsilon(1, -1)$,

which is marked in Fig. 2.1(c), corresponds to the secondary singular curve $\gamma(1, -1)$ below the primary curve $\gamma(1)$ in Fig. 3.3. If we zoom into each secondary structure of a primary window in the exit-velocity fractals of Fig. 2.1, we will see secondary window sequences which cascade to the right, i.e. the cascading direction of secondary window sequences is reversed from that of the primary window sequence. The reason for this is that in the map's $|m_\infty|$ fractal (see Fig. 3.2), the cascading direction of secondary sequences of singular curves is reversed from that of the primary sequence as we have explained before. The exit-velocity fractals of the PDE, the ODE and the map in Fig. 2.1 can be zoomed further, and all their microscopic structures can be inferred from the map's singular curves in Fig. 3.2, or from the map's $|m_\infty|$ fractal in Fig. 3.1 in general. One may notice that singularity peaks in the exit-velocity graphs appear only for the map and the ODEs, but not for the PDEs (see Fig. 2.1). Near such singularity peaks, the two solitary waves collide and coalesce, which makes our reduced ODE model (2.3) invalid. This explains the difference in those regions of the exit-velocity graphs between the ODEs and the PDEs.

From the map, we can obtain another important piece of information on the PDE/ODE's fractal as the initial solitary-wave separation $\Delta\xi_0$ (i.e. ζ_0) varies. In the present equal-amplitude initial conditions (2.16) and (2.18), if $\Delta\xi_0$ takes other (large) values, we can easily see from (4.1) that the values of $q_0 = m_0$ are independent of $\Delta\xi_0$. This means that the exit-velocity fractal of the map [see Fig. 2.1(c)] will remain the same for different initial solitary-wave separations, which in turn implies the same for the exit-velocity fractals in the PDE/ODEs. This is a surprising fact, and it has been confirmed by our direct PDE/ODE simulations. It is noted that this fact does not hold for the unequal-amplitude initial conditions (2.17) because (q_0, m_0) in such cases will depend on $\Delta\xi_0$, see (2.22).

In addition to the above qualitative understanding of the exit-velocity fractals in the PDEs and ODEs, we can further obtain the scaling properties of these fractals, i.e. we can determine quantitatively how the fractal structures in the PDEs and ODEs change as the parameter ε varies. For this purpose, we notice that the map's $|m_\infty|$ fractal at the intersection with λ^ε on the right half plane lies between two accumulation points, $(q_a, q_a) = (0.741, 0.741)$ and $(q_b, q_b) = (1.271, 1.271)$ on $\gamma(1, -1, -1, -1, ...)$ and $\gamma(1, 1, 1, 1, ...)$ respectively (see Fig. 4.1). In view of the initial-condition connection (4.1), the corresponding ψ_0 values of these two accumulation points are

(4.2) $\psi_L = -\mathrm{atan}(2q_b\pi^{-1/3}\varepsilon^{1/3}), \quad \psi_R = -\mathrm{atan}(2q_a\pi^{-1/3}\varepsilon^{1/3}).$

These ψ_L and ψ_R values are the left and right boundaries of the map's exit-velocity fractal on the negative $\Delta\phi_0$ axis [see Fig. 2.1(c)], and they are the map's predictions for the fractal regions in the PDEs/ODEs. These formulae show that $\psi_{L,R} \to 0$ as $\varepsilon \to 0^+$, which means that the whole fractal region shrinks to $\psi_0 = 0$ as $\varepsilon \to 0^+$. Notice that when $\varepsilon = 0$, the ODE solution $\zeta(\tau)$ under the equal-amplitude initial conditions (2.19) develops finite-time singularity at $\psi_0 = 0$, where $\mathrm{Re}(C_0) = 0, \mathrm{Im}(F_0) = 0$ (see Sec. 2). Thus when $\varepsilon \to 0^+$, the fractal region shrinks to the ψ_0 point which develops finite-time singularity in the integrable ODEs (see also [25]). Formulae (4.2) further show that this shrinking is at the rate of $\varepsilon^{1/3}$. To confirm this analytical prediction, we directly computed the exit-velocity fractals of the ODEs under the equal-amplitude initial conditions (2.19) as ε takes on smaller and smaller values of 0.1, 0.01, 0.001 and 0.0001, and the results are displayed in Fig. 4.2. We see that as $\varepsilon \to 0^+$, the ODE's fractal region indeed approaches $\psi_0 = 0$ [see Fig. 4.2(1-4)]. In addition, the fractal
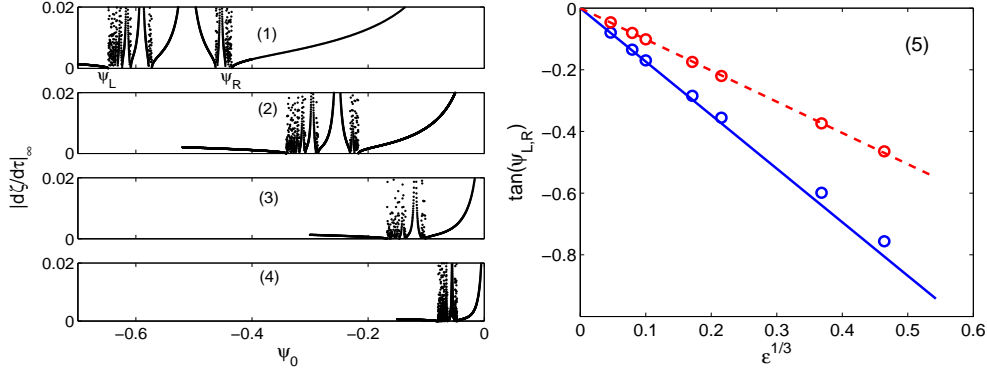
FIG. 4.2. *Left: change of fractal structures in the ODEs (2.3) as $\varepsilon \to 0^+$ under the equal-amplitude initial condition (2.19). The ε values are (1) 0.1; (2) 0.01; (3) 0.001 and (4) 0.0001 respectively. Labels ψ_L and ψ_R represent the left and right boundaries of the fractal region. Right: $\tan(\psi_L)$ (blue) and $\tan(\psi_R)$ (red) versus $\varepsilon^{1/3}$. The circles are data from the ODE simulations, and the straight lines are the analytical formulae (4.2) from the map.*

region's left and right boundaries ψ_L and ψ_R indeed shrink in proportion to $\varepsilon^{1/3}$. Furthermore, the constants of proportion match the analytical values in Eq. (4.2) as well [see Fig. 4.2(5)]. Similar agreement has also been found for PDE fractals, see [26].

The comparison in Fig. 4.2(5) indicates that for the present equal-amplitude initial conditions, the map's predictions are asymptotically accurate as $\varepsilon \to 0^+$. This is not surprising, as the fractal region here lies near $\psi_0 = 0$ when $|\varepsilon| \ll 1$. In this case, we can easily see from the definitions (2.6) and (2.7) that $E_0 \ll 1$, $M_0 \ll 1$ and $M_0/E_0 \ll 1$ for the present initial conditions when ψ_0 lies inside the fractal region. Thus the assumptions for the derivation of the map (2.9)-(2.10) are satisfied, and consequently the map's predictions are asymptotically accurate. For unequal-amplitude initial conditions (2.21), however, the assumption $M_0/E_0 \ll 1$ will not be met in general, thus the map's predictions will not be asymptotically accurate (even though they are still qualitatively accurate), see the next section for details.

4.2. The case of unequal-amplitude initial conditions. Now we consider the second case of unequal-amplitude initial conditions (2.17). In this case, the corresponding curve of the map's initial values in the (q_0, m_0) plane can be seen from (2.22) as

$$(4.3) \quad \lambda^{\varepsilon} = \{(q_0, m_0) : q_0 = -T(\psi_0)S(\psi_0)\varepsilon^{-1/3}, \ m_0 = T(\psi_0)\varepsilon^{-1/3}, \ \psi_0 \in [0, 2\pi]\},$$

where $T(\psi_0)$ is defined in (2.23), $S(\psi_0)$ given by (2.11), and the other involved parameters specified in (2.21). Here $H < 0$ in the entire interval of $\psi_0 \in [0, 2\pi]$, thus no restriction on ψ_0 is needed [27]. These curves at two ε values $\varepsilon_1 = 0.01$ and $\varepsilon_2 = 0.005$ are displayed in Fig. 4.3. Each λ^{ε} is a closed curve, and it intersects a singular curve $\gamma(\mathbf{a})$ twice. Let us denote the ψ_0 values at the two intersections as $\psi_1^{\varepsilon}(\mathbf{a})$ and $\psi_2^{\varepsilon}(\mathbf{a})$, with $\psi_1^{\varepsilon}(\mathbf{a}) < \psi_2^{\varepsilon}(\mathbf{a})$. These $\psi_{1,2}^{\varepsilon}(\mathbf{a})$ values are the singularity peaks of infinite height in the exit-velocity fractal of the map [see Fig. 2.2(c)]. On the singular curve γ_0, the intersection points would be denoted as ψ_1^{ε} and ψ_2^{ε}. As $\varepsilon \to 0^+$, these intersections are such that $q_0 \to +\infty$ in the right half plane and $q_0 \to 0^-$ in the left half plane. This behavior can be readily understood by examining the intersections of λ^{ε} with

the horizontal and vertical axes. The intersections with the horizontal axis are such that $m_0 = 0$. In view of (4.3) as well as the expression (2.23) for $T(\psi_0)$, we see that these intersections occur when $T(\psi_0) = 0$, i.e. when $\psi_0 = 0$ and π, regardless of the ε values. Note that under the present initial conditions,

$$(4.4) \quad q_A \equiv -\lim_{\psi_0 \to 0} T(\psi_0)S(\psi_0) = 0.962, \quad q_B \equiv -\lim_{\psi_0 \to \pi} T(\psi_0)S(\psi_0) = 0.641,$$

thus these two intersections on the horizontal axis are $(q_A \varepsilon^{-1/3}, 0)$ and $(q_B \varepsilon^{-1/3}, 0)$, which move to $(+\infty, 0)$ as $\varepsilon \to 0^+$. Similarly, the intersections of λ^ε with the vertical axis occur when $S(\psi_0) = 0$, i.e. when $\psi_A = 1.988$ and $\psi_B = 2.871$, regardless of the ε values. Then the two intersection points on the vertical axis are $[0, T(\psi_A)\varepsilon^{-1/3}]$ and $[0, T(\psi_B)\varepsilon^{-1/3}]$, which approach $(0, -\infty)$ as $\varepsilon \to 0^+$.

With the help of the map's singular curves as well as the initial-condition curve λ^ε in Fig. 4.3, we can now understand the map's exit-velocity fractal in Fig. 2.2(c), and hence the PDE/ODEs' exit-velocity fractals in Fig. 2.2(a, b). For these initial conditions, $\varepsilon = 0.001$ (see Sec. 2), and the initial-value curve λ^ε goes outside the box of Fig. 4.3 (thus not displayed). Instead, we will use the curve λ^{ε_2} in Fig. 4.3 (with $\varepsilon_2 = 0.005$) as a qualitative guide. The curve λ^ε in the first quadrant [above the accumulation curve $\gamma(1, 1, \ldots)$] corresponds roughly to $\psi_0 \in (\pi, 2\pi)$. This segment of λ^ε does not intersect with any singular curves, thus its corresponding exit-velocity graph would be smooth (in Fig. 2.2, this segment of the graph is not shown). The right intersection point of λ^ε with $\gamma(1, 1, \ldots)$ is where $\psi_1^\varepsilon(1, 1, \ldots) \approx 0$. This intersection corresponds to the left edge of the map's exit-velocity fractal in Fig. 2.2(c). From this intersection point down (leftward), λ^ε passes through the primary sequence of singular curves (in the reverse order), which corresponds to the primary sequence of singularity peaks starting from $\Delta\phi_0 \approx 0$ rightward (in the reverse order) in Fig. 2.2(c). The singularity peaks $\psi_1^\varepsilon(1)$ and $\psi_1^\varepsilon(1, 1)$ in this primary sequence are marked in Fig. 2.2(c), which correspond to lower intersections of λ^ε with primary singular curves $\gamma(1)$ and $\gamma(1, 1)$. At the lower intersection of λ^ε with the vertical axis, $\psi_1^\varepsilon = \psi_A = 1.988$, which is labeled in Fig. 2.2(c). From this lower vertical intersection point leftward, λ^ε passes through a thick band of singular curves, which corresponds to the structures right after the peak of ψ_1^ε in Fig. 2.2(c) (these structures are not well resolved and only a few vertical points are visible). After this thick band, λ^ε turns around (upward) and passes through another thick band of singular curves in the left half plane, which corresponds to the structures between the label '(c)' and the first major peak to its right in Fig. 2.2(c) (again these structures are not well resolved). The curve λ^ε crosses the vertical axis again (upper intersection) at $\psi_2^\varepsilon = \psi_B = 2.871$, which is labeled in Fig. 2.2(c). From this upper vertical intersection rightward, λ^ε passes through the primary sequence of singular curves again (in forward order), which corresponds to the primary sequence of singularity peaks from ψ_2^ε rightward and ending at $\psi_2^\varepsilon(1, 1, \ldots) \approx \pi$ in Fig. 2.2(c). From this correspondence between the initial-value curve λ^ε and the map's exit-velocity fractal in Fig. 2.2(c), a good and clear understanding of the exit-velocity fractals in the PDEs/ODEs [see Fig. 2.2(a, b)] is then reached.

From the previous section, we know that when $q_0 \to +\infty$, the map's secondary singular curves below each primary singular curve approach this primary curve. In addition, it is easy to see that all singular curves in the left half plane approach γ_0 (the vertical axis) when $q_0 \to 0^-$. Then in view of the small-ε asymptotics of curve λ^ε described above, we see that as $\varepsilon \to 0^+$, the intersections of λ^ε with the map's singular curves approach the primary sequence $\{\gamma_0, \gamma(1), \gamma(1, 1), \gamma(1, 1, 1), \ldots\}$. As
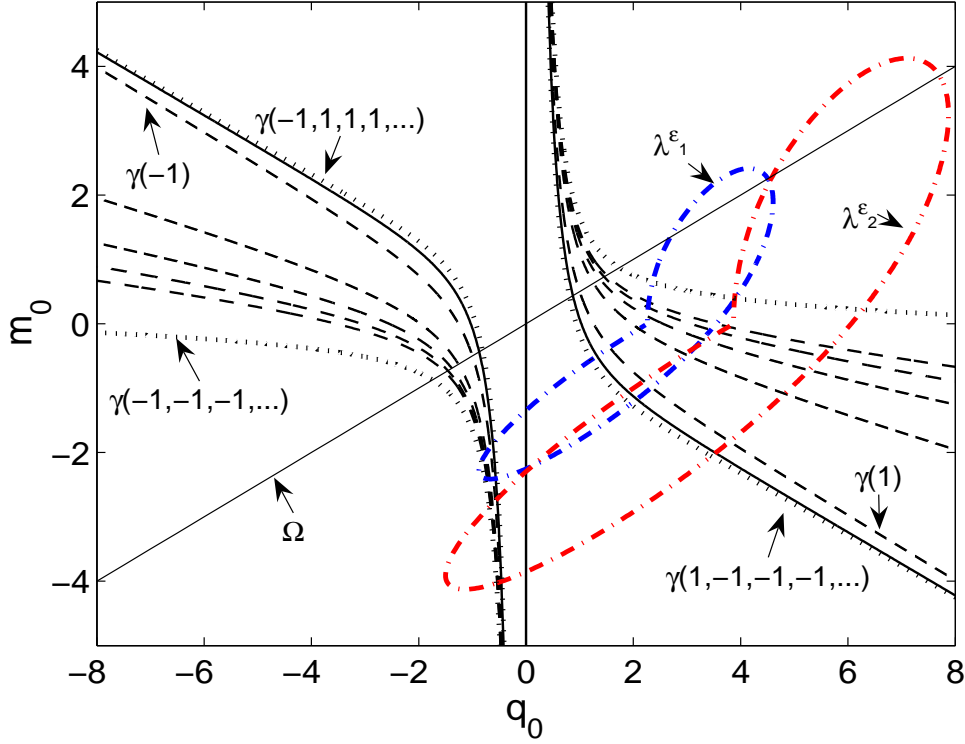
Fig. 4.3. *Curves of the map's initial points (4.3) corresponding to the unequal-amplitude initial conditions (2.21) at two ε values: $\varepsilon_1 = 0.01$ (blue) and $\varepsilon_2 = 0.005$ (red). Some singular curves are also shown by the same notations as in Fig. 4.1.*

a result, when $\varepsilon \to 0^+$, the exit-velocity fractals in the PDEs/ODEs will converge to certain discrete ψ_0 values whose corresponding (q_0, m_0) points fall on the above primary sequence. As was explained in [27], such discrete ψ_0 values are precisely the initial-condition points whose ζ-orbit in the integrable ODE system (2.3) develops finite-time singularities (this fact will be re-established again later in this section).

In addition to the above qualitative descriptions of the PDE/ODE's fractals (see Fig. 2.2), we can further determine how these fractal structures change quantitatively as $\varepsilon \to 0^+$. For instance, we can determine how the singularity peaks in the ODEs' exit-velocity fractal of Fig. 2.2(b) move as ε varies [the PDE's fractal does not have singularity peaks but only counterpart structures, see Fig. 2.2(a)]. This can be done because we know how the curve λ^ε moves with ε [see Eq. (4.3) and Fig. 4.3]. In addition, its intersections with singular curves of the map have either $q_0 \to +\infty$ (in the right half plane) or $q_0 \to 0^-$ (in the left half plane), where the asymptotics of singular curves have been derived in the previous section. Thus when the (q_0, m_0) relation of the curve λ^ε in (4.3) is inserted into the asymptotic equations of singular curves and all variables are expressed in terms of the control parameter ψ_0, quantitative changes of singularity peaks in the ODEs' exit-velocity fractals will be obtained. After simple algebra, we get the following asymptotic results in the limit of $\varepsilon \to 0^+$:

$$(4.5) \qquad\qquad \psi_1^\varepsilon = \psi_A, \quad \psi_2^\varepsilon = \psi_B,$$

(4.6) $\psi_k^\varepsilon(1, \mathbf{a}) = \psi_k^0(1, \mathbf{a}) + A_k(\mathbf{a})\varepsilon + \dots,$

(4.7) $\psi_k^\varepsilon(1, \mathbf{a}, -1, \hat{\mathbf{a}}) = \psi_k^0(1, \mathbf{a}) + G_k(\mathbf{a})\varepsilon^{1/2} + H_k(\mathbf{a}, \hat{\mathbf{a}})\varepsilon^{5/6} + \dots,$

(4.8) $\psi_k^\varepsilon(-1, \hat{\mathbf{a}}) = \psi_k^0 + P_k\varepsilon^{1/2} + Q_k(\hat{\mathbf{a}})\varepsilon^{5/6} + \dots.$

Here $\mathbf{a} = (a_1, ..., a_n)$, $a_1 = ... = a_n = 1$, $\hat{\mathbf{a}}$ is an arbitrary finite binary sequence, A_k, G_k, H_k, Q_k are constants whose values depend on the binary sequences behind them, P_k are $\hat{\mathbf{a}}$-independent constants, and $k = 1, 2$. If $n = 0$, then $\mathbf{a}$ is empty (which is allowed). Eq. (4.5) indicates that the singularity points ψ_k^ε in the ODEs' fractal [see Fig. 2.2(b)] are ε-independent. Actually these ψ_k^ε points in the ODEs/PDEs do depend weakly on ε, but this weak ε-dependence can not be captured by our map since it is beyond the asymptotic validity of the map. Eq. (4.6) describes how a primary singularity point approaches its integrable counterpart as $\varepsilon \to 0^+$, and this convergence is at the uniform rate of $O(\varepsilon)$. Relations (4.7) and (4.8) describe how the secondary structure of a primary singularity point approaches the integrable counterpart of this singularity point, and this convergence is at the uniform rate of $O(\varepsilon^{1/2})$. The length of the secondary structure, on the other hand, shrinks at the rate of $O(\varepsilon^{5/6})$. By substituting the (q_0, m_0) relation of (4.3) into the asymptotic equations (3.17) of primary curves and taking the limit of $\varepsilon \to 0$, we see that

(4.9) $S(\psi_k^0(1, \mathbf{a})) = 2(n + 1), \quad S(\psi_k^0) = 0, \quad k = 1, 2.$

In addition, at these ψ_k^0 and $\psi_k^0(1, \mathbf{a})$ values, it is easy to check that $\mathrm{Re}(C_0) \neq 0$, thus solutions of the integrable ODEs develop finite-time singularities in $\zeta(\tau)$ (see Sec. 2 and [27]). Thus relations (4.7) and (4.8), together with Eq. (4.2) and the discussions below it, quantitatively prove that when $\varepsilon \to 0^+$, the fractal regions in the non-integrable ODEs shrink to the ψ_0 points which develop finite-time singularities in the integrable ODEs, as was originally observed numerically in [25].

Now we compare the above analytical ε-scaling laws for the exit-velocity fractals in the PDEs/ODEs with direct numerical simulation results. Comparisons with only ODE simulations will be performed, as PDE simulations at very small ε values are very expensive and time consuming. For the ease of comparison, we take a small segment of the exit-velocity fractal in the ODEs as marked in Fig. 2.2(b), which corresponds to the segment on the initial-value curve λ^ε containing the lower intersection with $\gamma(1)$ and its secondary structure. Then we monitor how this segment of the fractal moves as ε varies by directly simulating the ODEs (2.3). At three ε values of 0.002, 0.001 and 0.0005, these segments of the fractal structures in the ODEs are displayed in Fig. 4.4 (1-3) respectively. Here the vertical solid lines mark the singularity point $\psi^0(1)$ in the integrable ODE system, the vertical dashed lines mark the singularity point $\psi^\varepsilon(1)$ in the non-integrable ODEs (with non-zero ε), and labels $\psi_{L,R}^\varepsilon(1)$ mark the left and right ends of the secondary structure. It is seen from these figures that as $\varepsilon \to 0^+$, both $\psi^\varepsilon(1)$ and the secondary structure approach the singularity point $\psi^0(1)$ of the integrable ODEs (as predicted). To determine the convergence rates, the graphs of $\psi^\varepsilon(1) - \psi^0(1)$, $\psi_{L,R}^\varepsilon(1) - \psi^0(1)$ and $\psi_R^\varepsilon(1) - \psi_L^\varepsilon(1)$ at various values of ε are plotted in Fig. 4.4(a, b, c) respectively. It is seen that as $\varepsilon \to 0^+$, $\psi^\varepsilon(1) - \psi^0(1)$ approaches a linear function in ε, confirming the $O(\varepsilon)$-convergence of the primary singularity point $\psi^\varepsilon(1)$ toward the integrable singularity point $\psi^0(1)$ [see formula (4.6)]. Quantities $\psi_{L,R}^\varepsilon(1) - \psi^0(1)$ approach a linear function in $\varepsilon^{1/2}$, confirming the
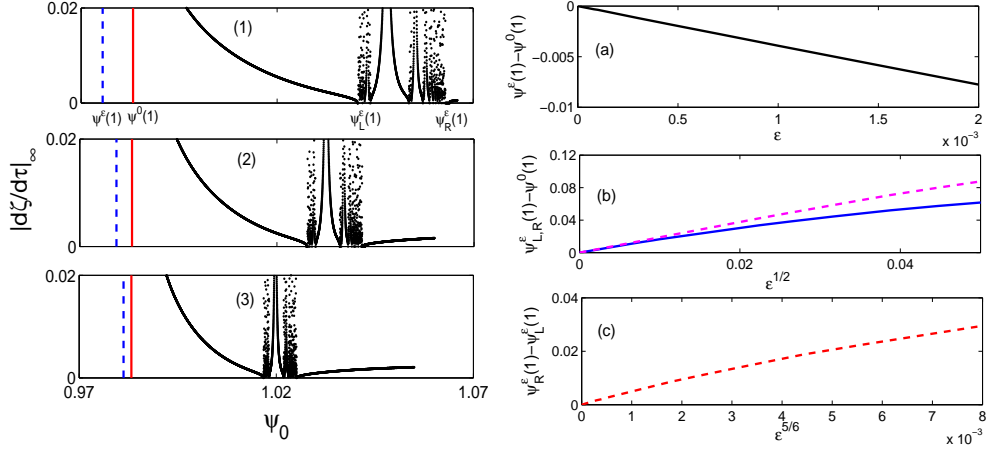
FIG. 4.4. *Left: segments of the ODE's fractal structures near the lower intersection between λ^ε and the primary singular curve $\gamma(1)$ under unequal-amplitude initial conditions (2.21) [this segment for $\varepsilon = 0.001$ was marked in the whole fractal structure of Fig. 2.2(b)]. The ε values are (1) 0.002; (2) 0.001 and (3) 0.0005. Right: (a) $\psi^\varepsilon(1) - \psi^0(1)$ versus ε; (b) $\psi_L^\varepsilon(1) - \psi^0(1)$ (blue) and $\psi_R^\varepsilon(1) - \psi^0(1)$ (red) versus $\varepsilon^{1/2}$; (c) $\psi_R^\varepsilon(1) - \psi_L^\varepsilon(1)$ versus $\varepsilon^{5/6}$.*

$O(\varepsilon^{1/2})$-convergence of the secondary structure toward the integrable singularity point $\psi^0(1)$ [see formula (4.7)]. In particular, it is seen that as $\varepsilon \to 0^+$, $\psi_L^\varepsilon(1) - \psi^0(1)$ and $\psi_R^\varepsilon(1) - \psi^0(1)$ approach linear functions in $\varepsilon^{1/2}$ with the same slope, confirming the formula (4.7) that the coefficient G_k of $\varepsilon^{1/2}$ is independent of the singular curves inside the secondary structure. The quantity $\psi_R^\varepsilon(1) - \psi_L^\varepsilon(1)$ approaches a linear function in $\varepsilon^{5/6}$, confirming the $O(\varepsilon^{5/6})$ shrinking rate of the length of the secondary structure [see (4.7)]. Thus our analytical predictions (4.6)-(4.8) on the order of convergence of ODE fractals as $\varepsilon \to 0^+$ are confirmed.

Quantitatively, the coefficients in front of the order of convergence in the analytical formulae (4.6)-(4.8) do not match numerical values though. For instance, in Fig. 4.4(a), the slope of $\psi^\varepsilon(1) - \psi^0(1)$ with respect to ε is found numerically to be -3.89, which differs from the analytical value of $A(1) = -5.12$ in formula (4.6). This means that in the present case of unequal-amplitude initial conditions (2.21), our analytical formulae (4.6)-(4.8) are not asymptotically accurate when $\varepsilon \ll 1$, which contrasts the equal-amplitude initial-condition case in Sec. 4.1 (where our analytical predictions were asymptotically accurate). The reason for this is that our map (2.9)-(2.10), or (2.13)-(2.14), was derived asymptotically under the condition of $M_n/E_n \ll 1$ [26, 27]. This condition was satisfied for the equal-amplitude initial conditions (2.16) (see Sec. 4.1), but is not satisfied for the unequal-amplitude initial conditions (2.21). Indeed, one can easily check that for ψ_0 values in the fractal regions of unequal-amplitude initial conditions (see Figs. 2.2 and 4.4), M_0/E_0 does not tend to zero as $\varepsilon \to 0$, thus the map's predictions become asymptotically inaccurate as we have just observed. Qualitatively, the map's predictions are still correct as Fig. 4.4 has demonstrated.

5. Dynamics of ODE and PDE solutions in the fractal structures. From the previous two sections, we have reached a clear and deep understanding on the fractal graphs of exit velocities in the ODEs and PDEs (see Figs. 2.1 and 2.2). In this section, we explain the solution dynamics of the ODEs and PDEs on these fractals. Notice that these fractals consist of hills of various widths. The 'center' of each hill

corresponds to a singular curve in the map's fractal, thus each hill can be identified by the binary sequence of that singular curve. We will show that once the binary sequence of a hill is given, then the solution dynamics of the ODEs and PDEs on that hill can be ascertained. Throughout this section, $\mathrm{sgn}(\varepsilon) = 1$, where fractal scatterings occur.

We first describe the ODE solution dynamics in the exit-velocity fractal. To demonstrate, we pick the hill of binary sequence $\mathbf{a} = (1, -1, 1)$ in the ODE's fractal for equal-amplitude initial conditions in Fig. 2.1(b). The segment which contains this hill is marked in that fractal. The amplification of this segment is shown in the inset of Fig. 5.1(a), where the widest hill is the one of this binary sequence $\mathbf{a}$. To examine the dynamics of ODE solutions on this hill, we pick three points on the hill with $\psi_a < \psi_b < \psi_c$, where the middle point ψ_b is the singularity peak point, and the other two points are on the two sides of this singularity point. These three points are marked in the inset of Fig. 5.1(a). At these three points, the ODE solutions $\zeta(t)$ and $\dot{\psi}(t)$ are displayed in Fig. 5.1(a, b) respectively. Here the time t has been rescaled back to the physical time for easy comparison with the PDE dynamics below. We see that at the singularity peak point ψ_b, the $\zeta(t)$ solution oscillates three times, then develops finite-time singularity at $t_c \approx 408$ and terminates there. Each local minimum of ζ is a saddle approach [27] where the separation between the two waves is the largest. Each local maximum of ζ is a 'bounce' point where the two waves are locally the closest and interact more strongly. The $\dot{\psi}(t)$ solution is mostly flat, except that it exhibits spikes at the three bounce points whose sign sequence is $(-1, 1, -1)$, which is opposite of the binary sequence $\mathbf{a}$. This $\dot{\psi}(t)$ solution also terminates at the finite-time singularity time t_c. At the other two points ψ_a and ψ_c on the two sides of the singularity peak ψ_b, the ODE solutions do not develop finite-time singularities. From Fig. 5.1(a, b), we see that these solutions are almost indistinguishable from the singular solution of ψ_b up to the singularity time t_c. At $t \approx t_c$, the $\zeta(t)$ solutions in both cases have a global maximum, where the two waves are the closest and interact most strongly. This time was called the *collision time* in [25]. Beyond this time, the $\zeta(t)$ solutions of ψ_a and ψ_c both go to $-\infty$ with finite speed. The $\dot{\psi}$ solutions of ψ_a and ψ_c approach constants as $t \to \infty$, but these asymptotic constants have opposite signs: the asymptotic constant for ψ_a at the left side of the singularity peak is positive, while that for ψ_c at the right side of the singularity peak is negative. At other points on this hill, the ODE solution dynamics is qualitatively similar to the ones above. From these examples, we can draw general conclusions for the ODE dynamics on a hill of an arbitrary binary sequence $\mathbf{a} = (a_0, a_1, a_2, \ldots, a_n)$ in the exit-velocity fractal. At the singularity peak of the hill, the $\zeta(t)$ solution oscillates $n + 1$ times (i.e. the two waves bounce with each other $n + 1$ times), and then approaches infinity at a finite time t_c and terminates. Here $n + 1$ is the length of the binary sequence $\mathbf{a}$. The $-\dot{\psi}$ solution exhibits spikes at the $n + 1$ bounce points before the singularity time t_c, whose sign sequence is $\mathbf{a}$. At other points of the hill, the ODE solutions are almost indistinguishable from this singular solution up to the singularity time t_c. The time t_c is approximately the collision time of all these ODE solutions. Beyond this collision time, all $\zeta(t)$ solutions go to $-\infty$, while all the $\dot{\psi}(t)$ solutions approach constants which have the same sign on the same side of the hill but opposite sign between the two sides.

From the above description of ODE dynamics on hills of exit-velocity fractals, we see that the 'physical' meaning of the binary sequence $\mathbf{a}$ of a hill in the ODE solutions is that $\mathbf{a}$ gives the sign sequence of the $-\dot{\psi}(t)$ solution at the bounce points before the

collision time. In addition, the difference in solution dynamics between the left and right sides of the hill is that the asymptotic constants of their $-\dot{\psi}(t)$ solutions have opposite signs. These two facts can be readily explained. First, from the definition (3.6), we know that the binary sequence $\mathbf{a}$ is the signs of $(q_0, q_1, \ldots, q_n)$, with $q_{n+1} = 0$. This orbit of the map corresponds to the ODE solution at the singularity peak of binary sequence $\mathbf{a}$ in the exit-velocity fractal. From Eqs. (2.9) and (2.12), we see that q_k has the sign of $-\Delta M_k$, where $\Delta M_k = M_{k+1} - M_k$, and M_k is the momentum value at the k-th saddle approach. Hence $\mathbf{a}$ is also the signs of $(-\Delta M_0, -\Delta M_1, \ldots, -\Delta M_n)$. Furthermore, from Ref. [27] [see Eqs. (3.4) and (5.6) in particular], $\mathrm{sgn}(-\Delta M_k)$ is the sign of $-\dot{\psi}$ at the k-th ζ-maximum (bounce point). Thus the binary sequence $\mathbf{a}$ is equal to the sign sequence of $-\dot{\psi}$ at the bounce points (before the singularity time or the collision time). Regarding the signs of $-\dot{\psi}(\infty)$ on the two sides of the hill, we notice from the map (2.13)-(2.14) that in the map's $|m_\infty|$ fractal in Figs. 3.1 and 3.2, when (q_0, m_0) is on the left (right) side of the vertical axis γ_0 and in its vicinity, q_∞ is positive (negative). Using the recursive relations (3.12)-(3.13) between singular curves and the orientation-preserving property of the inverse map $\mathcal{F}^{-1}$, we see that for (q_0, m_0) lying on the left (right) side of every singular curve (and in its vicinity), q_∞ is positive (negative). Notice that like bounce points above, the sign of q_∞ is the same as that of $-\dot{\psi}(\infty)$. In addition, the two sides of a hill in the ODE's exit-velocity fractal correspond to the two sides of the singular curve in the map's $|m_\infty|$ fractal. Thus the values of $-\dot{\psi}(\infty)$ on the two sides of a hill in the exit-velocity fractal have opposite signs. The specific signs of $-\dot{\psi}(\infty)$ on the two sides of the hill depend on how these two sides of the hill correspond to the two sides of the singular curve. If the left side of the hill corresponds to the left side of the singular curve, which is the case for hills starting from ψ_2^ε rightward in the unequal-initial-amplitude fractal of Fig. 2.2(b), then $-\dot{\psi}(\infty)$ would be positive (negative) on the left (right) side of the hill. But if the left side of the hill corresponds to the right side of the singular curve, which is the case for all hills in the equal-initial-amplitude fractal of Fig. 2.1(b) and the hills starting from ψ_1^ε leftward in the unequal-initial-amplitude fractal of Fig. 2.2(b), then $-\dot{\psi}(\infty)$ would be negative (positive) on the left (right) side of the hill.

The topic of higher interest to us is the interaction dynamics in the PDEs (2.1) rather than in the ODEs (2.3). So next we describe the PDE solution dynamics in the exit-velocity fractal. This PDE dynamics can be predicted from the ODE dynamics above. To illustrate, we take two $\Delta\phi_0$ values on the hill of binary sequence $\mathbf{a} = (1, -1, 1)$ in the PDE's equal-initial-amplitude fractal of Fig. 2.1(a), which correspond to the two ψ_0 values of the ODEs on the two sides of the singularity peak as marked in the inset of Fig. 5.1(a). For these two $\Delta\phi_0$ values, the PDE solutions are displayed in Fig. 5.1(c, d). We see that before the collision time $t_c \approx 408$, the two PDE solutions are almost identical with each other. In this time period, the two waves bounce three times. At the three bounce points, the left wave has higher, lower and higher amplitudes sequentially (when compared to the right wave). At the collision time, the two waves are the closest and interact most strongly. Afterwards, they separate from each other and escape to infinity. The main difference between the two PDE solutions is that, at the left $\Delta\phi_0$ value, the exiting right wave has higher amplitude, while at the right $\Delta\phi_0$ value, it is just the opposite. These behaviors are common for most of the points on this hill in the PDE's fractal. The only exception is a small region in the middle of this hill which corresponds to the singularity peak point and its immediate vicinity in the ODE's fractal [see inset of Fig. 5.1(a)]. In that region, the ζ solutions in the ODEs are either infinite or very large at the singularity time
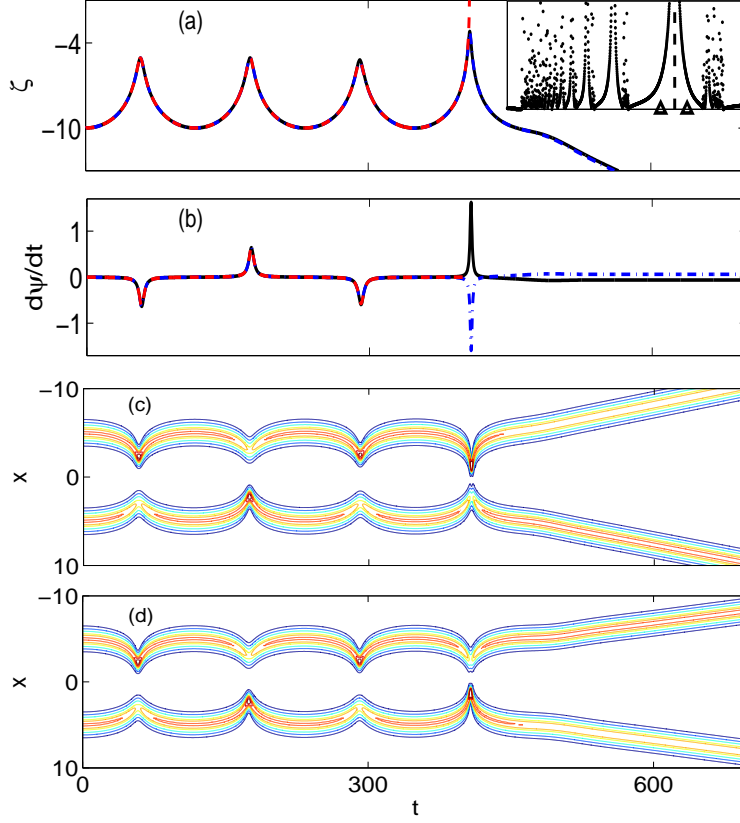
FIG. 5.1. *Dynamics of the ODE and PDE solutions on the hill of binary sequence* $\mathbf{a} = (1, -1, 1)$
*in the exit-velocity fractals for equal-amplitude initial conditions (2.16). The inset in (a) is an
amplification of the segment marked in the ODE fractal of Fig. 2.1(b), where the widest hill is the
one of binary sequence* $\mathbf{a} = (1, -1, 1)$. *Three locations* $\psi_a < \psi_b < \psi_c$ *on this hill are marked by two
triangles and a vertical dashed line, with the dashed line at* ψ_b *being the singularity peak point. The
ODE solutions at* ψ_a, ψ_b *and* ψ_c *are plotted as dash-dotted lines (blue), dashed lines (red) and solid
lines (black) in (a, b) respectively. The PDE solutions at points corresponding to* ψ_a *and* ψ_c *in the
PDE fractal of Fig. 2.1(a) are shown in (c, d) respectively (contour plots).*

or collision time, which implies that the two waves collide and coalesce. When this
happens, the reduced ODE model (2.3) and its predictions become invalid. Indeed in
the PDE's fractal, the central part of every hill dips down, which contrasts with the
ODE's fractal where the central part of each hill rises up to a peak of infinite height.

The PDE solutions in Fig. 5.1(c, d) directly correspond to the ODE solutions at
the two sides of the singularity peak in Fig. 5.1(a, b). In particular, the sign sequence
$\mathbf{a} = (1, -1, 1)$ of the ODE's $-\dot\psi(t)$ solution at the three bounce points directly implies
the "higher, lower, higher" amplitudes of the left wave at the three bounce points in
the PDE solution, and the negative (positive) $-\dot\psi(\infty)$ values at the left (right) side
of the singularity peak directly implies the lower (higher) amplitude of the exiting
left wave in the PDE solution. These connections can be readily explained. Let us
recall the relation $\Delta\phi_t = \Delta\beta$ as well as the fact that the propagation constant β is
directly related to the wave amplitude [25]. Then the sign of $-\dot\psi$, which is equal to
the sign of $-\Delta\beta = \beta_1 - \beta_2$, tells which of the two waves has higher amplitude. For the

cubic-quintic nonlinearity (2.15), the amplitude is an increasing function of β, thus positive $-\dot{\psi}$ means that the left wave has higher amplitude, which explains the above connections.

Based on the above PDE examples and general ODE dynamics, we can draw general conclusions for the PDE dynamics on a hill of an arbitrary binary sequence $\mathbf{a} = (a_0, a_1, a_2, \ldots, a_n)$ in the exit-velocity fractal. For all points on the hill, the PDE solutions are almost identical to each other up to the collision times (whose values are almost the same for the entire hill). Before the collision time, the two waves bounce $n + 1$ times. At each bounce point, the left wave has higher (lower) amplitude if the corresponding digit in the binary sequence $\mathbf{a}$ is 1 (-1). Thus the physical meaning of the binary sequence of a hill in the exit-velocity fractal is that it gives the sequence of relative amplitudes between the two waves at the bounce points before the collision time, with digit 1 (-1) meaning the left wave is higher (lower). At the collision time, the two waves are the closest and interact most strongly. For most of the points on the hill (except a small section in the middle), the two waves separate from each other after the collision time, and the exiting waves have opposite relative amplitudes on the two sides of the hill. The specific relative amplitudes of the two waves are determined by the sign of $-\dot{\psi}(\infty)$ which has been given above. The left wave will have higher (lower) amplitude if $-\dot{\psi}(\infty)$ is positive (negative).

6. The map for negative ε and its predictions for the PDE/ODE system. In this section, we consider the $\varepsilon < 0$ case. For the cubic-quintic nonlinearity (2.15), negative ε occurs when $\delta < 0$ [25]. In this case, we will show below that fractal scatterings can not occur. The map (2.13)-(2.14) for negative ε differs from that for positive ε by only a sign, but this makes a crucial difference. Now the map is

$$(6.1) \qquad \mathcal{F}\begin{pmatrix} q \\ m \end{pmatrix} = \begin{pmatrix} q + 2m + \frac{2sgn(q)}{q^2} \\ m + \frac{sgn(q)}{q^2} \end{pmatrix},$$

and

$$(6.2) \qquad \mathcal{F}^{-1}\begin{pmatrix} q \\ m \end{pmatrix} = \begin{pmatrix} q - 2m \\ m - \frac{sgn(q-2m)}{(q-2m)^2} \end{pmatrix}.$$

Notice that $\mathcal{F}$ and $\mathcal{F}^{-1}$ are still area-preserving and orientation preserving, but the singular-curve structure changes drastically. To see that, we start with the singular curves $\gamma(1)$ and $\gamma(-1)$, which are now

$$(6.3) \qquad \gamma(1) = \{(q_0, m_0) : m_0 = -q_0/2 - 1/q_0^2, \ q_0 > 0\},$$
$$(6.4) \qquad \gamma(-1) = \{(q_0, m_0) : m_0 = -q_0/2 + 1/q_0^2, \ q_0 < 0\}.$$

These two curves are shown in Fig. 6.1. We see that these curves are in the second and fourth quadrants. More importantly, they do not intersect with Ω. Because of this, each of these two singular curves has only one pre-image curve under the map of $\mathcal{F}^{-1}$. This contrasts with the $\varepsilon > 0$ case where each singular curve has two pre-image curves. The pre-image curves of $\gamma(1)$ and $\gamma(-1)$,

$$(6.5) \qquad \gamma(1, 1) = \mathcal{F}^{-1}(\gamma(1)), \quad \gamma(-1, -1) = \mathcal{F}^{-1}(\gamma(-1)),$$

are also shown in Fig. 6.1. They do not intersect with Ω either, thus have only one pre-image curve each as well. Repeating this process, then all the singular curves one
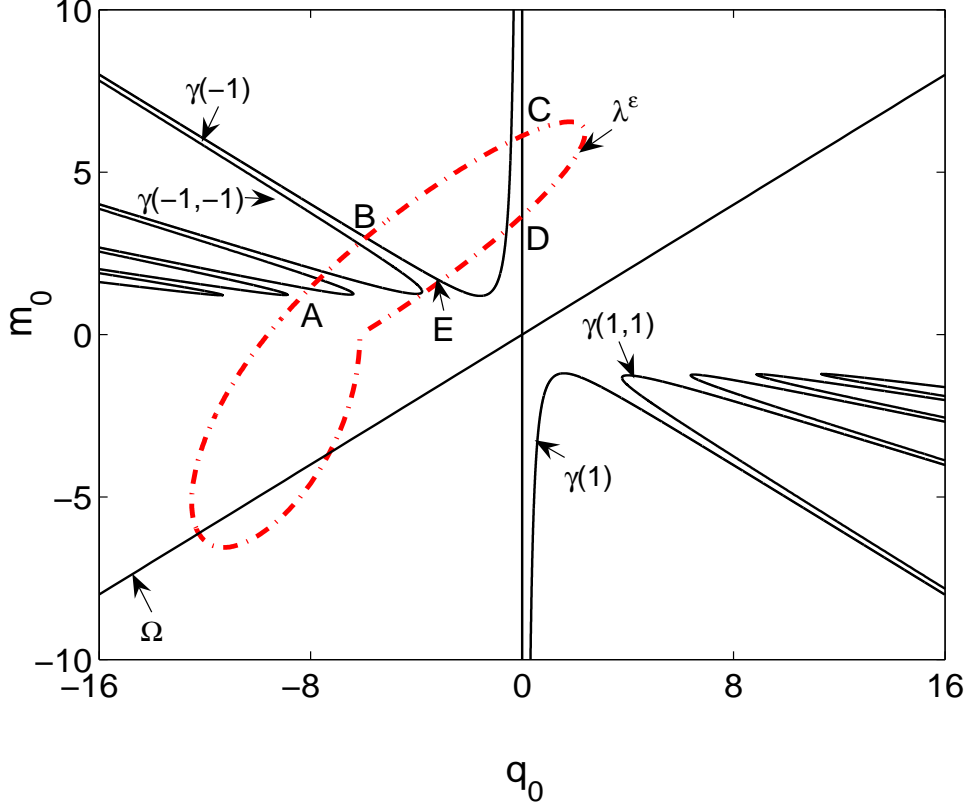
FIG. 6.1. *Singular curves of the map (2.13)-(2.14) for negative ε, as well as the initial-value curve λ^ε for unequal-amplitude initial conditions (2.21) with $\varepsilon = -0.001$. Five of the intersections of λ^ε with singular curves are marked by letters 'A, B, C, D, E'.*

can get, in addition to the vertical axis γ_0, are only two sequences

$$\{\gamma(-1),\ \gamma(-1,-1),\ \gamma(-1,-1,-1),\ ...\}$$

and

$$\{\gamma(1),\ \gamma(1,1),\ \gamma(1,1,1),\ ...\},$$

which are shown in Fig. 6.1. Obviously these two sequences can not develop fractals. If we draw the initial-value curves (4.1) and (4.3) in this same plane, these curves will intersect with only a finite number of singular curves. An example is shown in Fig. 6.1, where the unequal-amplitude initial conditions (2.21) and $\varepsilon = -0.001$ are taken. Thus the corresponding exit-velocity graph in the ψ_0 space will have a limited number of singularity peaks, which is precisely what we observed in Fig. 11(5)-(6) of Ref. [25].

Now we quantitatively compare the map's predictions with the ODE results for negative values of ε (comparison with the PDE results is expected to be similar, see Figs. 2.1 and 2.2). For this purpose, we take $\varepsilon = -0.001$ and the unequal-amplitude initial conditions (2.21) for the ODEs (2.3). In the PDE (2.1) with cubic-quintic nonlinearity (2.15), these ODE initial conditions correspond to $\delta = -0.0003$ and

unequal-amplitude initial conditions (2.17) [25]. From the direct simulations of these ODEs, the graph of exit-velocity $|\dot{\zeta}|_\infty$ versus the initial-phase difference ψ_0 is shown in Fig. 6.2(a). A finite number of singularity peaks can be seen, and this graph does not have a fractal structure. To obtain the map's predictions, we use the initial-value curve (4.3) for this case as shown in Fig. 6.1. For each point on this initial-value curve, we iterate the map (2.13)-(2.14) to infinity to obtain the exit velocity from Eq. (2.8). The results of the map's predictions are shown in Fig. 6.2(b). As can be seen, the map's prediction agrees with the ODE results very well. To better understand these graphs, we label five representative singularity peaks by letters 'A, B, C, D, E' in Fig. 6.2(b). Their corresponding points on the initial-value curve λ^ε of Fig. 6.1 are also labeled by the same letters. This connection makes it very easy to understand the exit-velocity graphs of Fig. 6.2. In particular, since λ^ε has 10 intersections with singular curves in Fig. 6.1, this explains why the exit-velocity graphs in Fig. 6.2 have 10 singularity peaks as well. One can further predict the dynamics of the ODE solution at each ψ_0 value in the exit-velocity graph of Fig. 6.2(a) in the same way as we did in the previous section. For instance, if ψ_0 is on a hill of binary sequence $\mathbf{a} = (-1, -1, -1)$ in the exit-velocity fractal of Fig. 6.2(a), then the $\zeta(t)$ solution will oscillate three times before the collision time. The $-\dot{\psi}$ solution will exhibit spikes at the three bounce points whose sign sequence is $\mathbf{a}$. After the collision time, the $\zeta(t)$ solution will go to $-\infty$, while the $\dot{\psi}(t)$ solution will approach a constant whose sign depends on which side of the hill the ψ_0 value is on. With this knowledge on the ODE solution, we can then predict the dynamics of the PDE solution, again in the same way as what we did in the previous section. If the two waves initially have equal amplitude, where the initial conditions for the ODEs are (2.19), then the initial-value curve λ^ε in (4.1) will only intersect one singular curve γ_0 (i.e. the vertical axis). In this case, the exit-velocity graph of the ODE will have a unique singularity point at $\psi_0 = 0$ and be smooth elsewhere. The corresponding dynamics of ODE and PDE solutions can be predicted in the same way as above. With these results, an intimate knowledge is then obtained for the wave interactions in the $\varepsilon < 0$ case.

7. Conclusion and discussion. In this paper, we analyzed the separatrix map which governs weak interactions of solitary waves in the generalized NLS equations. We showed that when $\varepsilon > 0$, this map exhibits a fractal structure which we delineated by tracking its singular curves. Then through this map's fractal as well as connections between the map and the ODEs/PDEs, we reached a very deep understanding on the fractal structures as well as their interaction dynamics in the ODEs and PDEs. In addition, we analytically determined how the ODE and PDE fractals change as the parameter ε varies, and showed that these predictions agree well with the numerical results. Furthermore, we proved a claim made earlier in [25] that fractal structures in the ODEs/PDEs for $\varepsilon > 0$ bifurcate from the singularity points in the integrable ODEs. When $\varepsilon < 0$, we showed that the separatrix map does not possess a fractal structure, hence fractal scatterings can not occur in the corresponding ODEs and PDEs.

Gathering all our results, we can now give a precise criterion for the existence of fractal scatterings in weak interactions of solitary waves in the generalized nonlinear Schrödinger equations. When $|\varepsilon| \ll 1$, fractal scatterings will occur if and only if the following two conditions are met:

1. $\varepsilon > 0$;
2. The map's initial-condition curve λ^ε [see (4.1) and (4.3) for instance], under the restriction of $H < 0$, intersects the map's fractal region (see Figs. 3.1, 4.1
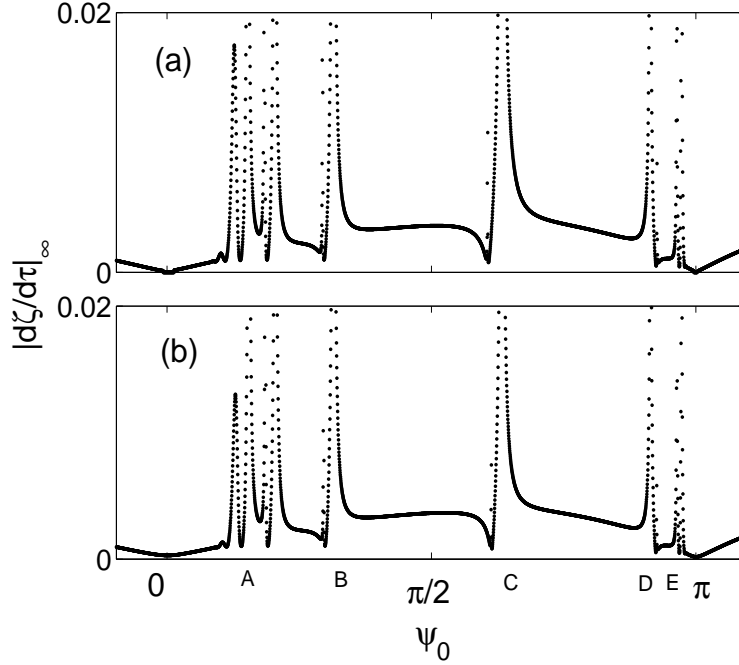
FIG. 6.2. *Comparison of the exit-velocity graphs from (a) ODE predictions, and (b) map predictions for $\varepsilon = -0.001$. The initial conditions of the ODEs are (2.21) for unequal-amplitude initial waves. Letters 'A, B, ...' are locations of some singularity peaks in (b), which correspond to the intersections of λ^ε with singular curves in Fig. 6.1 (marked by the same letters).*

and 4.3).

When this criterion is met (i.e. fractal scatterings occur), we can accurately predict the fractal structure as well as the interaction dynamics in the exit-velocity graph by simply drawing the initial-condition curve λ^ε on the map's $|m_\infty|$ fractal of Fig. 3.1. Thus, by now we have provided a simple answer to a complicated fractal-scattering problem in weak wave interactions.

The only discrepancy between the PDE's exit-velocity graph and our ODE/map predictions is at the middle part of each hill, where the ODE's and map's graphs exhibit peaks of infinite height, but the PDE's graph dips down instead (see Figs. 2.1 and 2.2). In those parameter regions, the two waves come together and interact strongly, which makes our reduced ODE model invalid. We have performed preliminary numerical investigations of the PDEs at the middle part of each hill in the exit-velocity graph, and found that the dips in those regions are not smooth. Inside each dip, we found finer structures which are also fractal-like! These fractal-like structures inside each dip are apparently the product of strong wave interactions, thus should be related to fractal scatterings in solitary wave collisions as reported in [11, 12, 13, 14]. Detailed investigations of finer structures inside dips of the PDE's exit-velocity graph lie outside the scope of this paper, and will be left for future studies.

REFERENCES

[1] M.J. Ablowitz and H. Segur, *Solitons and the Inverse Scattering Transform*, SIAM, Philadelphia, 1981.

[2] A. Hasegawa and Y. Kodama, *Solitons in Optical Communications*, Clarendon, Oxford, 1995.

[3] V. I. Karpman and V. V. Solov'ev, "A perturbation theory for soliton systems", Physica D 3, 142-164 (1981).

[4] V.S. Gerdjikov, D.J. Kaup, I.M. Uzunov and E.G. Evstatiev, "Asymptotic Behavior of N-Soliton Trains of the Nonlinear Schrödinger Equation", Phys. Rev. Lett. 77, 3943 - 3946 (1996).

[5] V. S. Gerdjikov, E. V. Doktorov and J. Yang, "Adiabatic Interaction of N-Ultrashort Solitons: Universality of the Complex Toda Chain Model." Phys. Rev. E. 64, 056617 (2001).

[6] J. Yang, "Suppression of Manakov-Soliton Interference in Optical Fibers", Phys. Rev. E 65, 036606 (2002).

[7] Y. Kodama, "On integrable systems with higher order corrections", Phys. Lett. A 107, 245-249 (1985).

[8] A. S. Fokas and Q.M. Liu, "Asymptotic Integrability of Water Waves", Phys. Rev. Lett. 77, 2347 - 2351 (1996).

[9] T.R. Marchant, "Asymptotic solitons for a higher-order modified Korteweg-de Vries equation", Phys. Rev. E 66, 046623 (2002).

[10] M.J. Ablowitz, M.D. Kruskal and J.F. Ladik, "Solitary Wave Collisions", SIAM J. Appl. Math. 36, 428 (1979).

[11] D. K. Campbell, J. S. Schonfeld, and C. A. Wingate, "Resonant structure in kink-antikink interactions in ϕ^4 theory", Physica D 9, 1-32 (1983).

[12] P. Anninos, S. Oliveira, and R. A. Matzner, "Fractal structure in the scalar $\lambda(\phi^2-1)^2$ theory", Phys. Rev. D 44, 1147-1160, 1991.

[13] Y. S. Kivshar, Z. Fei, and L. Vázquez, "Resonant soliton-impurity interactions", Phys. Rev. Lett. 67, 1177-1180, 1991.

[14] J. Yang and Y. Tan, "Fractal structure in the collision of vector solitons", Phys. Rev. Lett. 85, 3624-3627, 2000.

[15] B.A. Malomed, *Variational methods in nonlinear fiber optics and related fields*, Progress in Optics Volume 43, North-Holland, 2002.

[16] Z. Fei, Y. S. Kivshar, and L. Váquez, "Resonant kink-impurity interactions in the sine-Gordon model", Phys. Rev. A 45, 6019-6030, 1992.

[17] T. Ueda and W. L. Kath, "Dynamics of coupled solitons in nonlinear optical fibers", Phys. Rev. A 42, 563 (1990).

[18] Y. Tan and J. Yang, "Complexity and regularity of vector-soliton collisions", Phys. Rev. E. 64, 056616 (2001).

[19] R. H. Goodman and R. Haberman, "Interaction of sine-Gordon kinks with defects: The two-bounce resonance", Phys. D. 195, pp. 303–323 (2004).

[20] R. H. Goodman and R. Haberman, "Vector soliton interactions in birefringent optical fibers", Phys. Rev. E 71, pp. 056605 (2005).

[21] R. H. Goodman and R. Haberman, "Kink-antikink collisions in the phi-four equation: The n-bounce resonance and the separatrix map", SIAM J. Appl. Dyn. Sys. 4, pp. 1195-1228 (2005).

[22] R. H. Goodman and R. Haberman, "Chaotic Scattering and the n-Bounce Resonance in Solitary-Wave Interactions", Phys. Rev. Lett. 98, 104103 (2007).

[23] S.V. Dmitriev, Yu.S. Kivshar, and T. Shigenari, "Fractal structures and multiparticle effects in soliton scattering", Phys. Rev. E 64, 056613, 2001.

[24] S.V. Dmitriev and T. Shigenari, "Short-lived two-soliton bound states in weakly perturbed nonlinear Schrödinger equation", Chaos 12, 324 (2002).

[25] Y. Zhu and J. Yang, "Universal fractal structures in the weak interaction of solitary waves in generalized nonlinear Schrödinger equations", Phys. Rev. E, 75 (2007), 036605.

[26] Y. Zhu R. Haberman and J. Yang, "A universal map for fractal structures in weak solitary wave interactions", Phys. Rev. Lett., 100, 143901 (2008).

[27] Y. Zhu R. Haberman and J. Yang, "A Universal Separatrix Map for Weak Interactions of Solitary Waves in Generalized Nonlinear Schrödinger Equations", Physica D 237, 2411(2008).

[28] R. H. Goodman, "Chaotic scattering in solitary wave interactions: A singular iterated-map description", Chaos, 18, 023113(2008)

[29] D.K. Arrowsmith and C.M. Place, *An introduction to Dynamical Systems*, Cambridge University Press, Cambridge, 1990.